JOURNAL OF SOLID STATE CHEMISTRY **135,** 235–255 (1998)
ARTICLE NO. SC977621

Electron Microscopic and X-Ray Structural Analysis of the Layered Crystals $TaReSe_4$: Structure, Defect Structure, and Microstructure, Including Rotation Twins

V. V. Volkov,*,†,[1] J. Van Landuyt,*,[2] S. Amelinckx,* V. S. Pervov,† and E. V. Makhonina†

*EMAT, University of Antwerp (RUCA), Groenenborgerlaan 171, B-2020 Antwerpen, Belgium; †N. S. Kurnakov Institute of General and Inorganic Chemistry, Russian Academy of Sciences, Leninsky Prospect 31, 117907 Moscow, GSP-1, Russian Federation

Received April 9, 1997; accepted September 10, 1997

A combined X-ray and electron microscopy analysis was used for structure and microstructure characterisation of the newly synthesized layered compound $TaReSe_4$. This compound crystallizes in the hexagonal system with lattice parameters $a = b = 3.32130(4)$, $c = 12.95910(16)$ Å and $\alpha = \beta = 90^\circ$, $\gamma = 120^\circ$ (space group $P6_3/mmc$, $Z = 1$, $D_x = 9.161$ g/cm^3). X-ray powder structure refinement confirmed $TaReSe_4$ as a full structural analogue of 2H-WSe_2. The defect structure of $TaReSe_4$ is characterized by the presence of a number of rotation twins with twist angles 9.43°, 13.17°, 17.89°, 21.78°, and 27.79°. Apart from these, a high density of 2D-defects was observed in the (0001) plane. In some cases these results in the formation of an almost periodical "superlattice" with a period along the c axis of about 60 Å. A simple geometrical theory for the rotations- (R-) twins on the hexagonal lattice has been developed as well. Experimental results on R-twins fit very well the predicted ones based on an explicit formulae derived in this work. Along with the main phase a small admixture of a superstructure phase (<2%) with lattice parameters $a' \approx b' \approx 2a$, $c' \approx c/2$ and epitaxially grown on $TaReSe_4$ was found. It was identified from selected area diffraction patterns as the triclinic $ReSe_2$ phase. A self-consistent structure-physical model for the coexistence of R-twins, 2D-defects and prismatic cluster defects in the material is proposed and discussed in view of the experimental results. © 1998 Academic Press

1. INTRODUCTION

Because of their nearly two-dimensional structural features many layered compounds exhibit a number of interesting physical properties; in particular, large anisotropy of the optical properties, charge electron transfer [1], metal–semiconductor phase transitions [2], superconductivity [3], and some others. Layered disulfides and diselenides of the transition metals as well as their derivatives—intercalated compounds—are of great interest not only for the physics of low-dimensional systems, but also for practical applications: they can be used as solid lubricants, cathodes of small recycling current sources, as effective catalysts [4], etc.

It is common knowledge that the isostructural and isoelectronic dichalcogenides MoS_2, WS_2, and WSe_2 can hardly be intercalated [1, 5] because their lowest metal orbital d_{z^2} is fully occupied by two electrons in a trigonal prismatic crystal field. On the other hand, the substances with only one electron in the lowest d_{z^2} orbital, such as NbX_2 and TaX_2 (X = S, Se) can easily form intercalated compounds including incommensurate structures [6, 7]. In the latter case the energy gain is caused by the electron charge transfer effect from the dopants (or doping guest layers) to the host matrix.

The synthesized powdered compound $TaReSe_4$ (TRS) [8] also belongs to the same class of the layered chalcogenides. In contrast to the expected results, as it was shown in [9], it can be intercalated at least with In and Sn. Thus, the intercalation mechanism of the complex matrix of $TaReSe_4$ remains unclear. On the other hand, the material possesses a very useful combination of physical properties for applications, i.e., excellent lubricant properties and semimetal conductivity [8], in contrast to insulating MoS_2. To our knowledge the crystal structure of TRS is not well determined yet, since there is only one short report on the structure of TRS [10] based on the analysis of the intensity of 17 main reflections in a powder XRD pattern.

Therefore the present work was aimed at a more detailed examination of the structural peculiarities of $TaReSe_4$ powder and their relation to the excellent lubricant properties of the material. It will be demonstrated how the combined use of HREM–TEM–ED, SEM, EDX, and powder XRD methods can be applied to the structure, microstructure, and defect structure analysis of the new material, available only in powder. We shall show as well that the experimental results on rotation R-twins found in TRS are in good

[1] On leave from N. S. Kurnakov Institute.
[2] To whom correspondence should be addressed.

0022-4596/98 $25.00

agreement with the predicted ones obtained from explicit analytic formulae for R-twins derived in the present work. Both of them fit very well the results of numerical calculations based on the 'coincidence site lattice' theory of W. Bollmann [11].

2. EXPERIMENTAL

Powdered samples of $TaReSe_4$ were prepared from high purity elements: Re 99.99%, Ta 99.72%, and Se 99.995%. Mixtures of the elements of nominal composition were encapsulated in evacuated fused quartz tubes and subjected to a two-step sintering procedure by the standard solid state reaction method at 670°C (15 h) and 870°C (10 h). After grinding the samples were annealed at 900°C (150 h) followed by cooling at a rate of 50°C/h. The details of the synthesis procedure are described in [8].

High resolution electron microscopy (HREM) and electron diffraction (ED) studies of the material were carried out using a JEOL 4000EX microscope operating at 400 kV. The tilting experiments needed to reconstruct the reciprocal space were carried out with a 200 kV Philips CM-20 electron microscope. Sample preparation was very straightforward: the microcrystals were crushed and glued onto copper grids. For HREM observations we mostly used specimens prepared by ion beam milling of a sample of $TaReSe_4$ powder mixed with epoxy glue. Such specimens made it possible to avoid the preferential orientation due to strong natural anistropy of the platelet microcrystals and to obtain cross-section HREM images containing the *c*-axis.

To characterize the surface morphology, the elemental composition, and the lattice parameters of the phases of interest, scanning electron microscopy (SEM), energy dispersive X-ray (EDX), and X-ray powder diffraction (XRD) analyses were performed. For this purpose a JEOL GSM-T220A scanning electron microscope equipped with an EDX KEVEX system for microprobe elemental analysis and an X-ray powder diffractometer Philips PW3710 (Cu$K\alpha$ radiation) equipped with a PC 486/DX2 for structural refinement by the Rietveld method were used.

3. RESULTS

3.1. SEM and EDX Analysis

The typical morphology of the small crystallites and their sizes observed by SEM are depicted in Figs. 1a–1c. Small platelet crystals of black color have a hexagonal or truncated trigonal prismatic shape with a thickness not exceeding one micrometer, whereas lateral dimensions could be different—up to a few tens of micrometers. The local chemical composition of the different crystallites was reproducible within the accuracy of EDX measurements ($\pm 2\%$) and almost independent of their size, corresponding well to the stoichiometric formula of $TaReSe_4$ (Fig. 1d).

3.2. Electron Diffraction, HREM, and Structural Model

Some ED patterns viewed along the main directions of the reciprocal space of TRS are shown in Figs. 2a–2c. All the reflections in these ED patterns can be indexed in the hexagonal system with the following approximate lattice parameters: $a = b = 3.30$, $c = 13.0$ Å, $\alpha = \beta = 90^\circ$, $\gamma = 120^\circ$. The ED pattern shown in Fig. 2d cannot be indexed in any simple way and will be discussed below in relation to a new specific type of 2D-defects found in the material. We shall refer to them below as rotation- (R-) twins. Analysis of the extinctions allowed us to derive the following reflection conditions:

$$hkil\text{: no conditions;} \quad hh(-2h)l : l = 2n;$$

$$h(-h)0l\text{: no conditions.}$$

Such conditions are consistent with the symmetry of two trigonal ($P3\bar{1}c$, $P31c$) and four hexagonal ($P6_3/mmc$, $P6\bar{2}c$, $P6_3mc$, $P6_322$) space groups [12]. Taking into account the expected density of the compound ($\rho = 9.15\,g/cm^3$) and the possible number of molecules in the unit cell ($Z = 1$), it is clear that the cations and anions should occupy only twofold and fourfold positions regardless of the space group used, for instance;

$$\tfrac{1}{2}(\mathrm{Ta} + \mathrm{Re})\text{: (2c)} \pm (\tfrac{1}{3}, \tfrac{2}{3}, \tfrac{1}{4})$$

$$\mathrm{Se}\text{: (4f)} \pm (\tfrac{1}{3}, \tfrac{2}{3}u; \tfrac{2}{3}, \tfrac{1}{3}, u + \tfrac{1}{2}),$$

where the (2c) positions are occupied by Ta and Re in equal proportion and u is the structure parameter to be refined. Notice that the choice of the space group is not critical because the positions chosen are common for all these space groups. Thus, the structure of $TaReSe_4$ is expected to be very similar to that of the $2H_b$-polytype of the layered MoS_2 ($u = 0.629$) or WS_2 ($u = 0.625$) and, moreover, to be isoelectronic to them. Indeed, the simulated ED patterns for the proposed structural model of $TaReSe_4$ with ideal value of parameter $u = 5/8 = 0.625$ have shown good qualitative agreement with the experimental ones (Figs. 2a–2c). An example of a high resolution image of $TaReSe_4$ taken along the $[11\bar{2}0]$ direction (Fig. 3) also confirms the validity of the structure model chosen (insets, Fig. 3). The stacking sequence of atoms in the $2H_b$-polytype $(a\gamma ac\alpha c)_n$ reproduces well the fine details of the HREM image (upper inset, Fig. 3). Notice that the local structure of TRS was found to contain a number of different types of defects. The smallest ones shown in Fig. 3 (we shall term them X and Y defects) have a tendency to form a cascade-like stacking, as shown in Fig. 3, in order to minimize the energy of lattice deformations. They are caused by the local self-intercalation by heavy cations or local atom displacements accompanied by a partial widening of the Van der Waals (VDW) gaps,

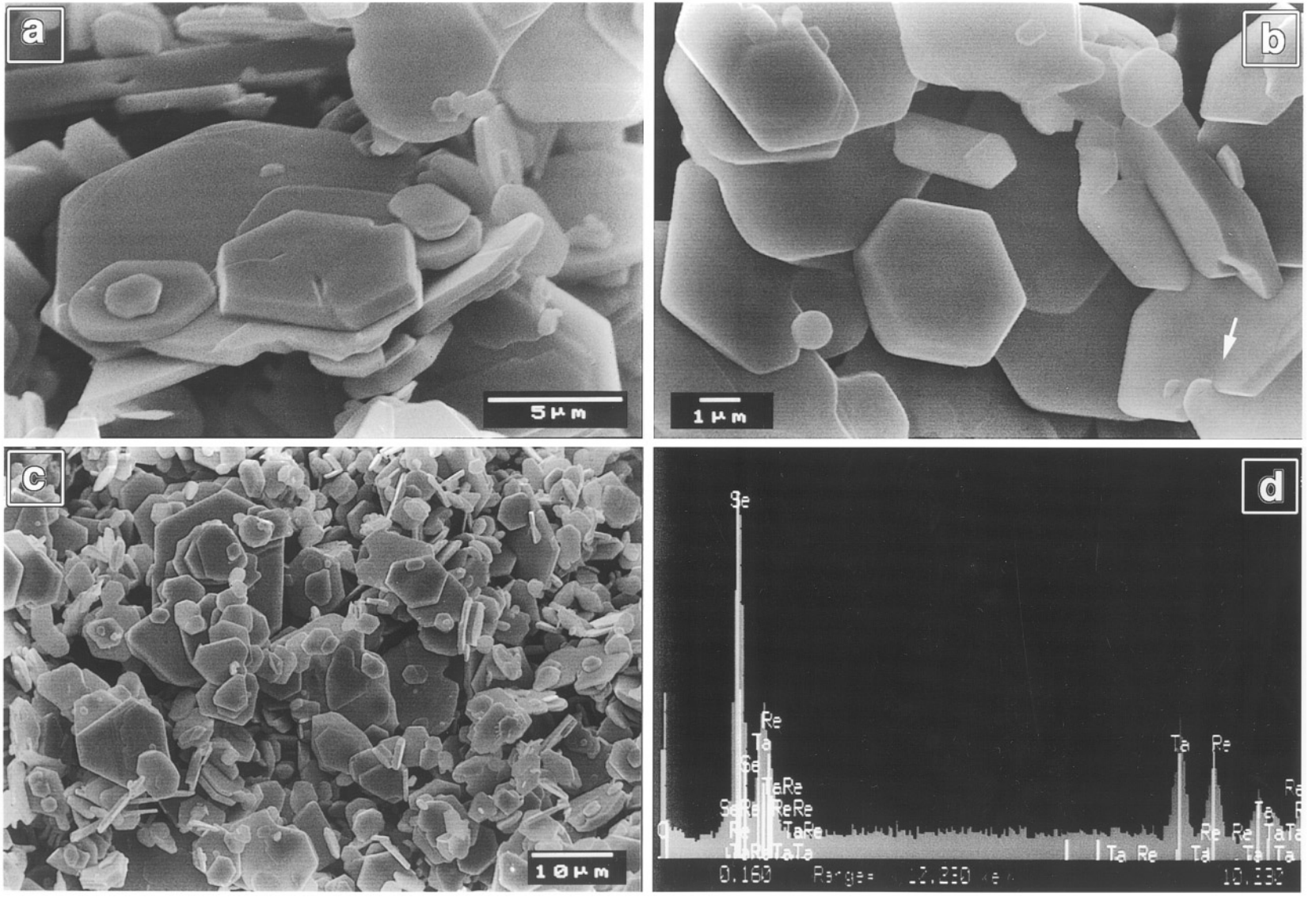

FIG. 1. Scanning electron microscope images of $TaReSe_4$: (a), (b) high magnification images; (c) overview of powder; (d) X-ray microanalysis of the same material. Note the platelet shape and steplike character of intergrowth of crystallites along the c-axis, including the presence of deformed and twinned crystallites (marked by arrow).

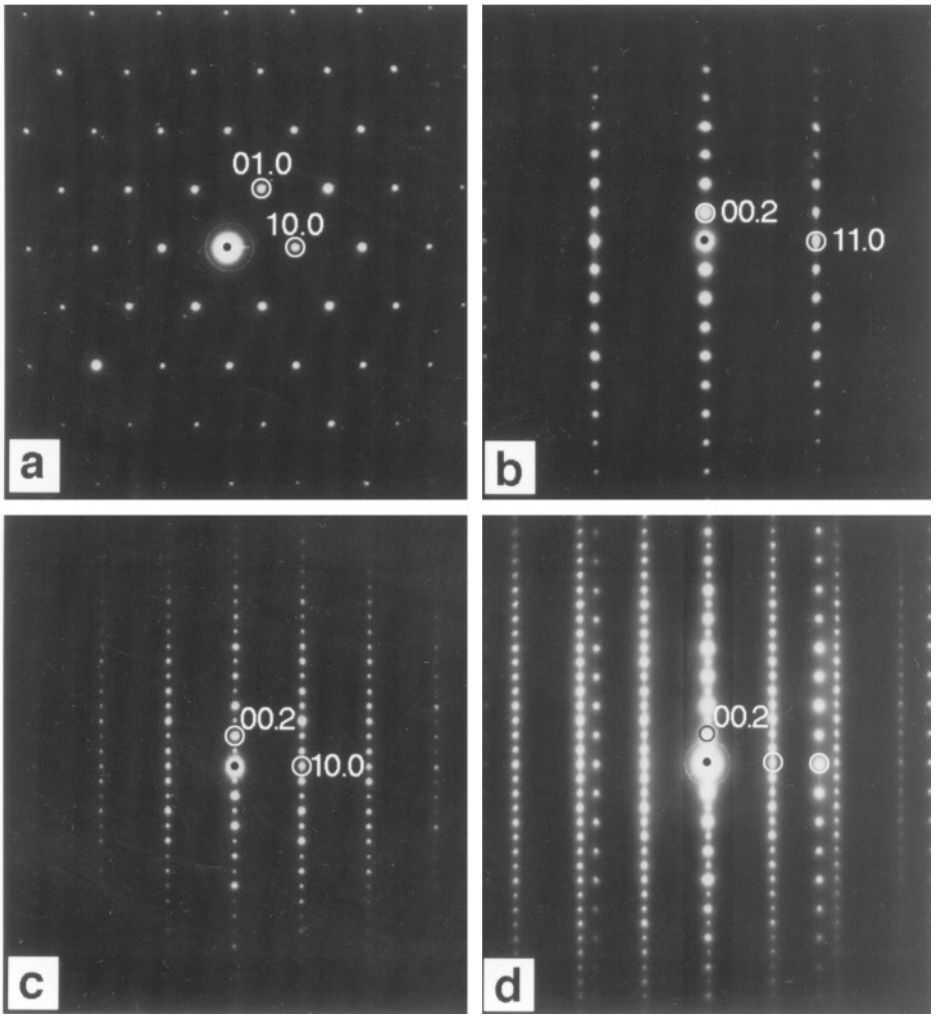

FIG. 2. Electron diffraction patterns of $TaReSe_4$ viewed along different directions: (a) [0001]; (b) [11$\bar{0}$0]; (c) [01$\bar{1}$0]. Weak reflections (0001) with $l = 2n + 1$ along c-axis in (c) are caused by double diffraction.

imaged as bright lines (Fig. 3). In many cases the defects can overlap, resulting in a highly perturbed lattice image. Under those circumstances a direct HREM image analysis is problematic. Notice that an alternative choice of possible Wyckoff positions for a structure model will be discussed below in relation with the observed defect microstructure of the material. Meanwhile, it should be mentioned that a 3R-$TaReSe_4$ polytype (analogue of 3R-WSe_2) was not observed during our TEM-ED experiments.

3.3. XRD Pattern and Structure Refinement

The results of electron microscopy observations have been directly used for the structure refinement of $TaReSe_4$, carried out on the basis of the powder XRD pattern shown in Fig. 4. For this purpose a full profile Rietveld analysis with the help of the program RIETAN-94 [13] was applied with the following conditions: space group $P6_3/mmc$, starting parameter $u = 0.625$, a block mode for the thermal

FIG. 3. High resolution images of the $TaReSe_4$ atomic structure viewed along the [112$\bar{0}$] direction: (a) higher magnification (in the insets: stacking sequence of atoms in $2H_b$-polytype (a γ a c α c)$_n$ and electron diffraction pattern); (b) lower magnification demonstrates the cascade stacking of extended defects caused by the local intercalation and partial disclosure of VDW-gaps (lines of white contrast). In the insets: structure model of $TaReSe_4$; calculated images corresponding to model at defocus -40 nm and thicknesses 2 and 3 nm; high magnification image of X-defects.

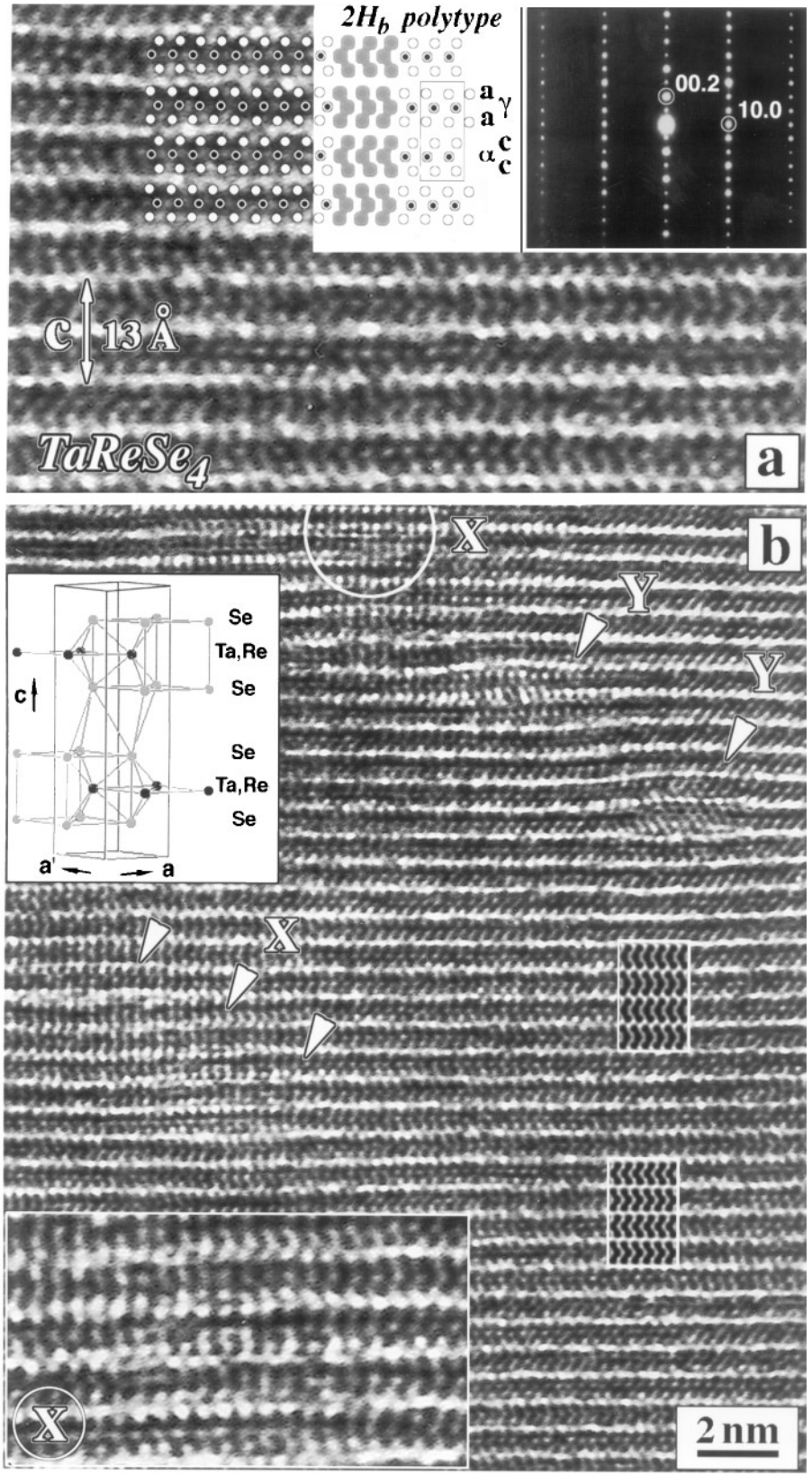
2H_b polytype
a
a
γ
α
c
c
00.2
10.0
c
13 Å
TaReSe4
a
b
X
Y
Y
Se
Ta,Re
Se
Se
Ta,Re
Se
c
a'
a
X
X
2 nm

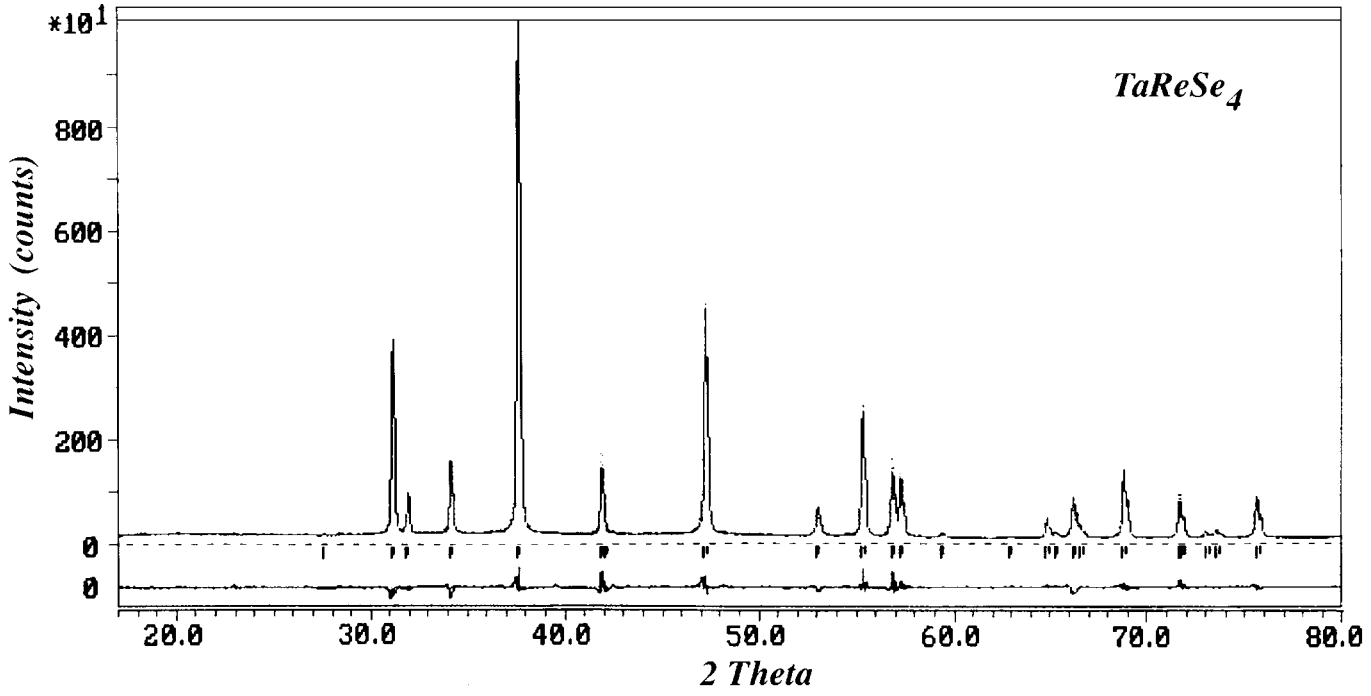

FIG. 4. The observed, calculated and difference X-ray patterns after structure refinement.

parameters of Se and Me atoms assuming [0001] preferential orientation. The refined lattice parameters are $a = b = 3.32130(4)$, $c = 12.95910(16)$ Å, $\alpha = \beta = 90$, $\gamma = 120^\circ$ ($Z = 1$, $D_x = 9.161$ g/cm^3). The residual R-factors were $RF = 2.18$, $RI = 3.46$, $R_p = 4.97$, $R_{wp} = 6.65\%$. The experimental and calculated XRD patterns as well as the residual pattern are shown in Fig. 4. The results of the calculations are collected in Tables 1a–1c. In accordance with the conclusions derived above from the ED patterns, Se atoms indeed occupy (4f) positions. The refined value $u = 0.621$ coincides well with that for WSe_2 ($u = 0.621$). Notice that the refined structure has $u = 0.621$ with reasonably small residual R-factors. Therefore the average structure of $TaReSe_4$ is expected to be the same as that of WSe_2 assuming the absence of any ordering of Ta and Re in the cation sublattice and stoichiometry. For this reason for instance the low angle reflection (0002) in XRD pattern was excluded from the refinement, since its intensity was strongly dependent on the annealing conditions and texture effects and contained a weak satellite line attributed later to the strongest reflection (100) of a small amount of $ReSe_2$ admixture revealed by local ED and EDX analysis. The real microstructure of TRS was found to be very interesting and to contain a number of types of defects caused by the lack of local nanoscale stoichiometry, as will be demonstrated below by the direct HREM image analysis.

Notice that for the class of layered chalcogenides under discussion, each layer consists of metal atoms (M) placed in trigonal prisms of six chalcogen atoms (X) in such a way that all three neighboring face-sharing chalcogen prisms remain empty. As a result each X–M–X layer is built of alternatingly empty and filled face sharing trigonal prisms (inset, Fig. 3). The parameter $\delta = (u - \frac{5}{8})$ can be used as a measure of the deformation of these prisms along

TABLE 1a
Main Crystallographic Parameters

Empirical formula	$TaReSe_4$	Cell constants (Å) :	
Crystal system	Hexagonal	a	3.32130(4)
Space group	$P6_3/mmc$	c	12.95910(16)
Color; habit	Black platelet; powder	Volume (Å^3) :	123.800(2)
Z	1	D_X (g cm^{-3})	9.161
Diffractometer	PW3710	$2\theta^\circ$ range	16–80°
Number of reflections	52	Number of variables	22
Radiation, λ(Å)	Cu$K\alpha_{1,2}$	RI, RF, R_P, R_{wP}	3.46, 2.18, 4.97, 6.65

TABLE 1b
Fractional Coordinates and Thermal Parameters of the Atoms in $TaReSe_4$

Atom	Site	x/a	y/b	z/c	B_{iso} (Å^2)	Occ.
Ta	2c	0.33333	0.66666	0.25	0.1(1)	0.5
Re	2c	0.33333	0.66666	0.25	0.1(1)	0.5
Se	4f	0.33333	0.66666	0.62112(8)	0.2(1)	1.0

TABLE 1c
Some Interatomic Distances (Å) in $TaReSe_4$

(Ta/Re)–Se × 6	2.5429(7)	Se–Se × 6	3.3213
(Ta/Re)–(Ta/Re) × 6	3.3213	Se–Se* × 6	3.6866(7)

the c-axis in the family of isostructural compounds MoS_2 ($u = 0.629$), WS_2 ($u = 0.625$), WSe_2 ($u = 0.621$), $Ta_{0.5}Re_{0.5}Se_2$ ($u = 0.621$), and $MoTe_2$ ($u = 0.621$). It seems that deformation of the chalcogen prisms along this row of compounds changes from a slight compression ($\delta > 0$) to a slight extension ($\delta < 0$) and can be related to the relative radii of the light and heavy atoms present. In the case of $Ta_{0.5}Re_{0.5}Se_2$ the main interatomic distances are the following: The shortest Re–Se or Ta–Se distances are 2.546(13) Å. Within the X–M–X layers the nearest Se–Se interatomic distances are 3.322(13) Å. Inside the Se_2Me_3 fragment the Se–Se distance in 3.350(13) Å; actually, this is the thickness of the X–M–X sandwich lamellae. Finally, the shortest Se–Se distances between two neighboring X–M–X lamellae were found to be 3.674(13) Å. The calculated width of the Van der Waals gap between the X–M–X lamellae in $Ta_{0.5}Re_{0.5}Se_2$ is 3.14 Å. It is smaller than that of MoS_2 (3.17Å) and $MoTe_2$ (3.38 Å), but equal to that of WSe_2.

The parameter $u = 0.621$ obtained in the present study differs from $u = 0.625$ obtained in (10). In our opinion the former is more accurate for two reasons. First, it was obtained by the more accurate method of full profile refinement. Second, the difference in Z number between W($Z = 74$) and Ta($Z = 73$), Re($Z = 75$) is equal only to 1. For cations in the $Ta_0.5Re_0.5Se_2$ structure the effective $Z = (73 + 75)/2 = 74$, i.e., the same as for W in the WSe_2 structure. Therefore from a physical point of view equal parameters $u = 0.621$ for both of these structures simply reflect a complete identity of their average structure caused by the equal average mass ($Z = 74$) and by the equal total cation charge ($W^{4+}W^{4+}$ and $Ta^{3+}Re^{5+}$) of the cation sublattice.

Notice that the isotropic thermal parameter of the Se atoms (Table 1b) is two times larger than that of the metal atoms. This formally implies a higher flexibility of the Se atoms, but in fact it may be directly related to the high density of 2-D defects discussed below and associated with transformations in anionic sublattice of TRS.

3.4. Defect Structure

The defect structure of $TaReSe_4$ is characterized by the presence of several types of defects occuring on the (0001) planes of hexagonal layered crystals, which we shall classify according to their dimensionality: (a) 2-D twist boundaries generated by rotation twins with a common c-axis; (b) 2-D "defect planes" characterized by a partial displacement vector of $R = a/3\langle 1\bar{1}00\rangle$ type, the most frequent type of extended defect found in $TaReSe_4$ with a linear density of 10^5–$10^6 cm^{-1}$ along the c-axis; (c) 1 D defects, predominantly perfect glide dislocations with Burgers vectors of the type $\mathbf{b} = a\langle 101\bar{0}\rangle$; and (d) extended defects of the prismatic type in (0001) planes caused by local intercalation in the VDW-gap between X–M–X sandwiches. The movement of glide dislocations (c) in (0001) planes was directly observed during our TEM experiments at room temperature using two-beam diffraction contrast under the conditions where $\mathbf{g} \cdot \mathbf{b} \neq 0$. They were concentrated around defect areas or inclusions and could even form a dislocation network. We do not intend to discuss them in detail, since the behavior of this type of defect is well described in (14). Therefore in the present paper we shall analyze only the (a), (b), and (d) defects found in TRS.

3.4.1. Rotation twins and superstructures. A number of rotation twins (R-twins) with a common c-axis, forming twist boundaries in the (0001) planes of TRS, were found during our TEM-ED experiments. They are not very frequent, since the major part of the material was relatively free of this type of 2-D defects. On the other hand, they were found to be very stable during the heating or cooling of specimens in the temperature range 90–1100 K. Therefore it was concluded that they are growth features. Some examples of complex SAED patterns, produced by such R-twins and viewed along the [0001] direction, are shown in Figs. 5–7. In particular, the SAED patterns in Fig. 5 reflect the case of 14° R-twins forming a nearly commensurate pattern. The HREM image in Fig. 5b confirms the nearly commensurate character of the superstructure. Alternatively it can be described as a moiré image formed by the twist boundary generated by R-twins with a "magic" misorientation angle. Examples where two different R-twins can be found within one crystallite are shown in Fig. 6. We shall show below that the interpretation of such patterns, including those in Figs. 7a and 7b, can be simplified when using the concept of geometrical moiré patterns, as shown in Figs. 7c and 7d. To make sure that such ED patterns do not correspond to the formation of nearly commensurate or commensurate superstructures in the bulk, a systematic TEM–HREM–SAED analysis has been applied to specimens of TRS prepared by ion beam milling, as described above, which enabled us to obtain information on cross-sections of platelet crystals. As can be seen from Fig. 8, typical ED patterns of R-twins cannot be indexed in a rational way, but can be considered as composite ones, exhibiting some "magic" angles, produced by the rotation of the hexagonal reciprocal lattice around the c^*-axis. Indeed, dark field (DF) imaging analysis of corresponding ED and SAED patterns, obtained by tilting around the c-axis, and experimental HREM images unambiguously indicate the presence of several R-twins parallel to the (0001) plane, always consistent with some "magic number" twist angles. The examples of cross-section mixed TEM–HREM images of 14° and 27° R-twins are shown in Figs. 9 and 10 respectively. For a DF-image in Fig. 10 the reflection $\mathbf{g}_{11\bar{2}0}$ was used. Analysis of HREM images of the interfacial atomic structure at twist boundaries led us to the conclusion that for 25°–27° R-twins in some

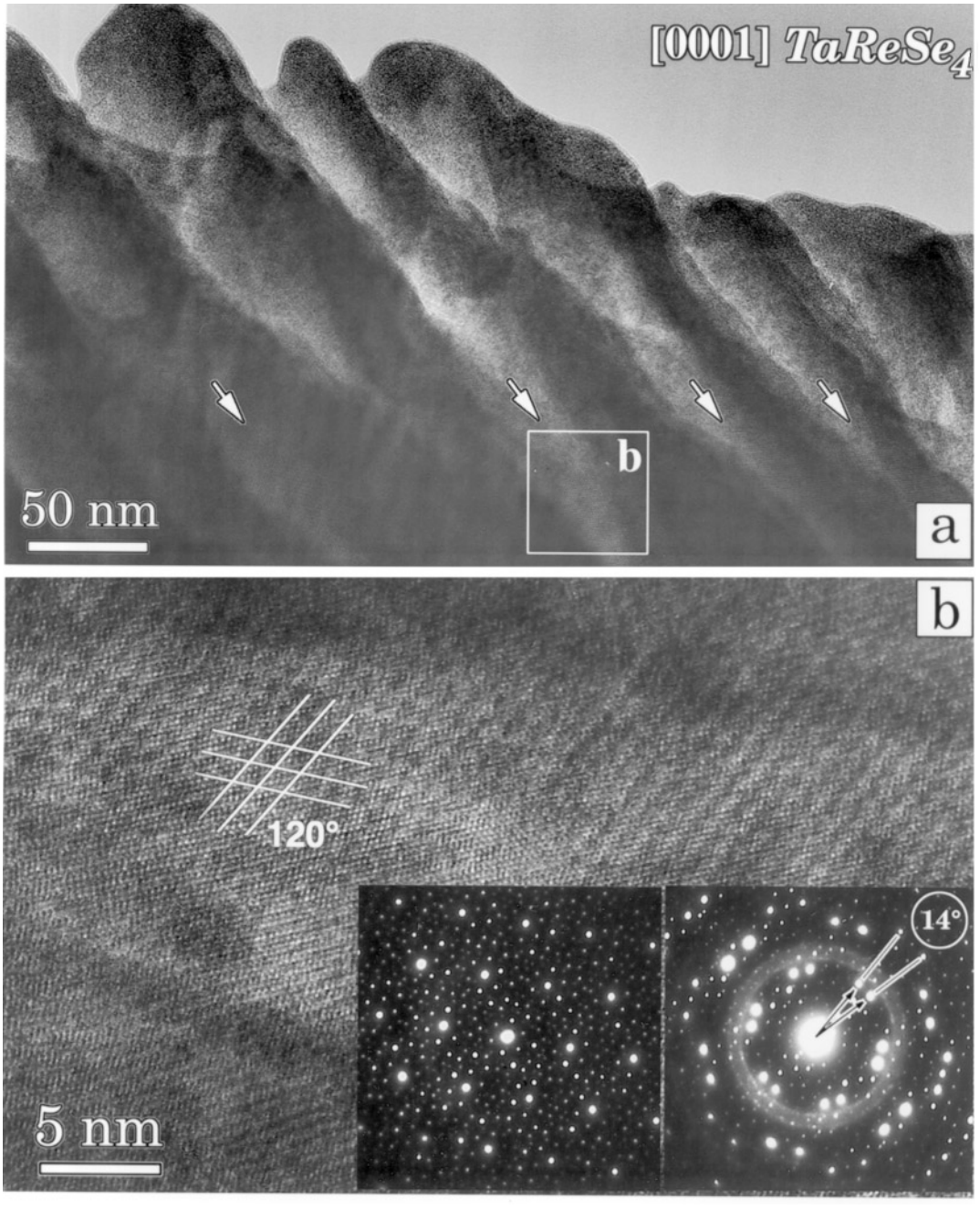

FIG. 5. Images of 14° R-twins viewed along common *c*-axis: (a) low magnification image: (b) HREM image of the selected *b*-area in (a). In the insets: nearly commensurate electron diffraction patterns along [0001] on the left side and after small specimen shift (right side).

cases the interface was rather more amorphous than the normal one, as shown in Fig. 10. Notice that the R-twins co-exist with 2-D defects, which will be discussed below. The twist boundaries occur approximately at the same distance along the *c*-axis as the 2-D defects (Fig. 9a). This suggests that they may have a common physical-chemical origin. It seems that the contact plane of the twist boundaries in $TaReSe_4$ on the atomic scale coincides with the VDW gap. One such example is depicted in the cross-section HREM image of the 14° twist boundary in Fig. 9c, where the VDW gaps are imaged as lines of bright contrast. Therefore in conclusion it is worth noticing, that the mechanism of formation of such unusual R-twins is presumable related to the reconstruction of the VDW gap structure, for instance via weakening or partial breaking of already weak chemical bonds across the gap.

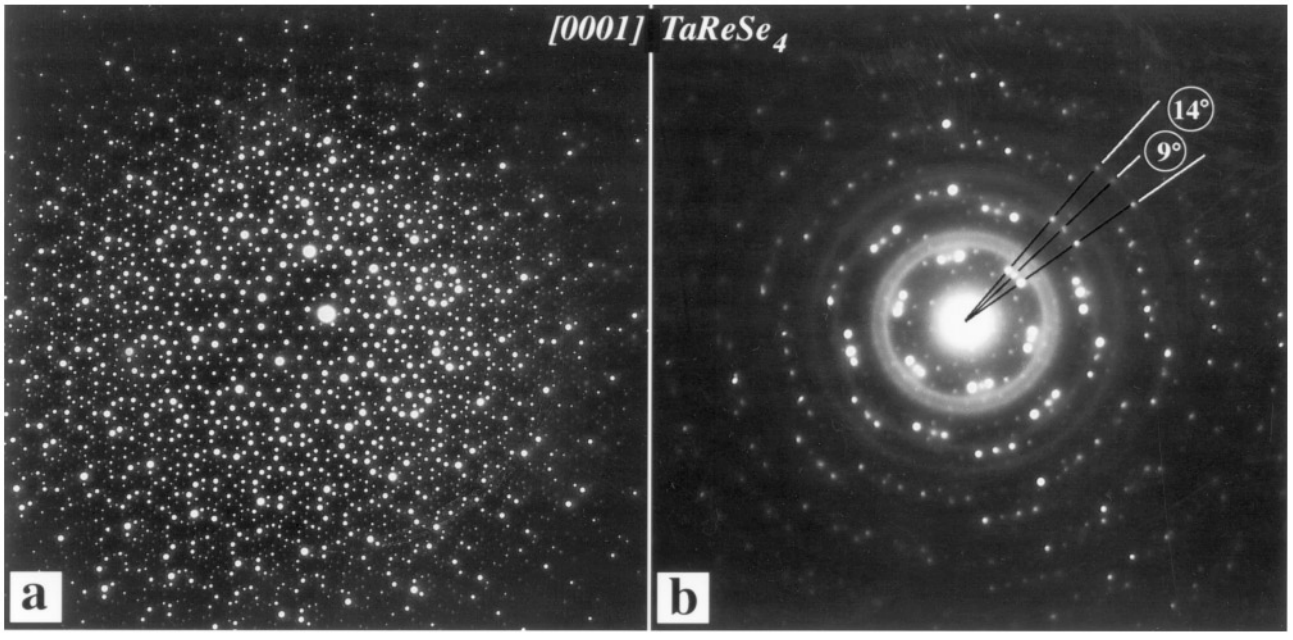

FIG. 6. Examples of complex composite diffraction patterns of TaReSe4 viewed along [0001]: (a) superposition of $25^\circ + 17.5^\circ$ R-twins; (b) superposition of $14^\circ + 9^\circ$ R-twins.

To rationalize the experimental data on R-twins we have developed a simple geometrical model, based on the concept of "two mirrors," which can be generalized to a 2-D twist boundary related to a coincidence site lattice (CSL) on close packed layers. The model allowed us to obtain exact analytical expressions for all possible "magic" angles of R-twins on a hexagonal lattice, which are in good agreement with the experimental data on TRS as well as in excellent fit with the numerical results of the O-lattice theory performed for the case of rotation CSL on (111) cubic plane [11].

3.4.2. Theory of rotation twins: "*Two mirrors*" *model.* For small twist angles the (0001) twist boundaries can be modelled as hexagonal grids of screw dislocations forming hexagonal cells of good fit. As the twist angle increases, the energy of the boundary at first increases because of the increase in dislocation density, which in turn causes a decrease of the areas of good fit. Both the self-energy and the interaction energy of the dislocation network contribute to the boundary energy. From an alternative point of view one can note that, as the twist angle increases, the fraction of the boundary covered by areas of good fit decreases and hence the free energy increases.

Above a certain twist angle, when the dislocation cores start overlapping, one can still consider regions of good fit and strongly perturbed regions. Intuitively it is clear that the fraction of the surface area covered by regions of good fit will increase since the density of coincidence sites increases with increasing angle. This would account for the decrease in energy with increasing twist angle above a certain critical twist angle. Therefore the density of the coincidence site lattice (CSL) as a function of the twist angle becomes the important parameter. However, only for a certain specific misorientation angle the local maxima of CSL density, corresponding to local minima in free energy, will occur, because the density of CSL is a highly oscillating function of the twist angle. Boundaries with twist angles, corresponding to local minima of free energy, will be preferable. Once the misorientation angle is locked in as such, a large energy barrier would have to be overcome in order to leave this minimum, for instance by rotational slip.

A coincidence lattice for two hexagonal arrays of sites can be generated by making coincide mirror related vectors of the two superimposed hexagonal lattices. Since a two-dimensional hexagonal lattice has two crystallographically different mirror planes (P_1, P_2 in Fig. 11), two different sets of mirror related rotation twins (R-twins), generating twist boundaries, have to be considered in general. Notice, that the results obtained will be valid both for the real and reciprocal hexagonal lattice.

Let n and m represent the number of steps along the basic directions $\mathbf{a}_1$ and $\mathbf{a}_2$ of the hexagonal lattice; the latter are shown as $\mathbf{a}_{10}$ and $\mathbf{a}_{01}$ in Fig. 11. All sites of the lattice can then be represented by vectors $\mathbf{a}_{nm} = n\mathbf{a}_1 + m\mathbf{a}_2$. The vector $\mathbf{a}_{nm}$ of the first lattice and its mirror image $\mathbf{a}^*_{nm} = \mathbf{P}_1\mathbf{a}_{nm} = m\mathbf{a}_1 + n\mathbf{a}_2$ of the second lattice with respect to the mirror plane P_1 (parallel to $\mathbf{a}_1 + \mathbf{a}_2$ in Fig. 11) will lead to the formation of a CSL only if the difference vector between

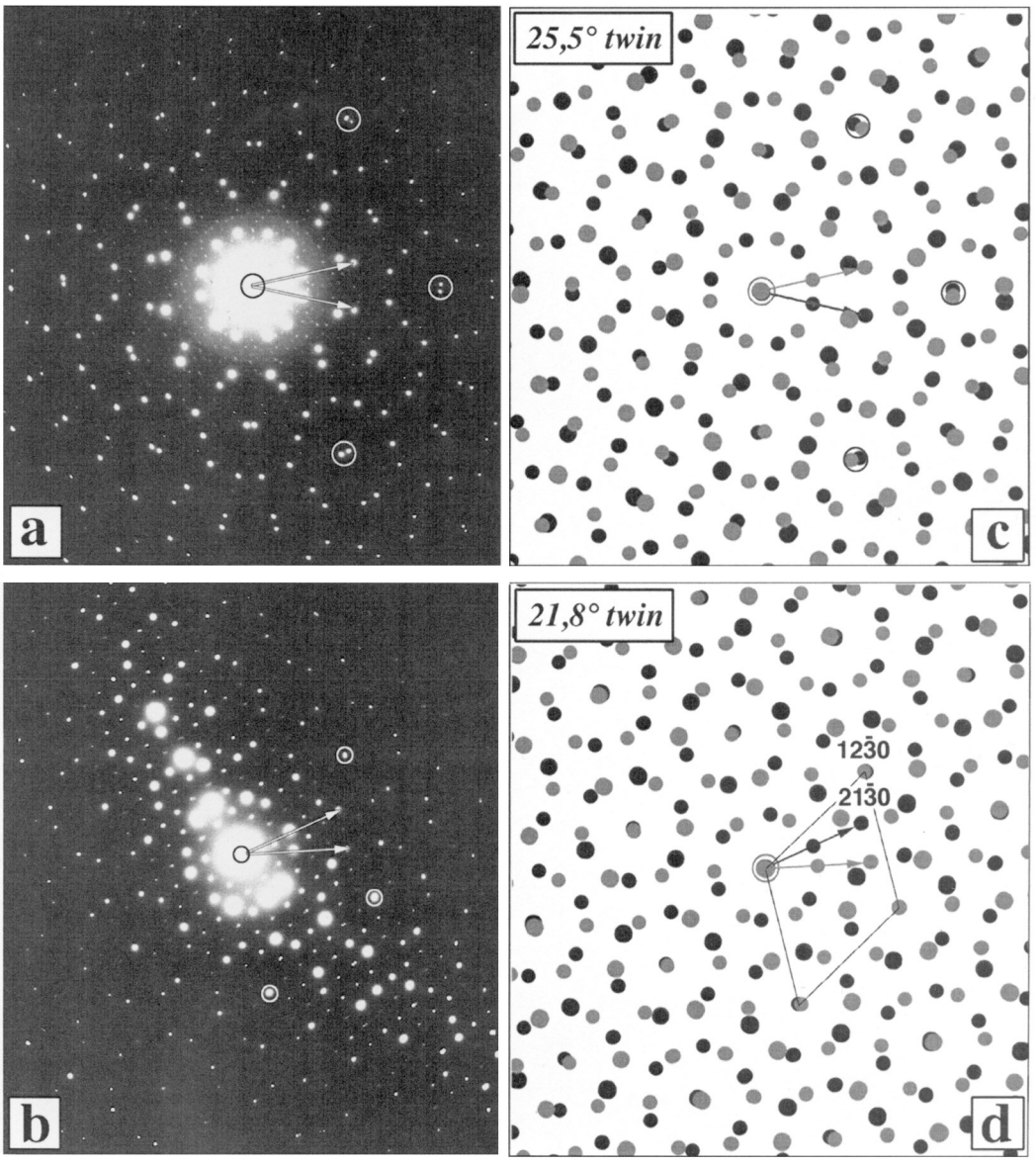

FIG. 7. SAED patterns of R-twins for the case of 25° (a) and 21° (b). Moiré patterns (c, d) of 25° and 21° R-twins were obtained by superposing masks of hexagonal point lattice.

these vectors (for instance, vector $\mathbf{r} = \mathbf{g}_1 - \mathbf{g}_2$, as shown in Fig. 11) is again a lattice vector $\mathbf{r}$:

$$\mathbf{r} = \mathbf{a}_{nm} - \mathbf{a}^*_{nm} = (\mathbf{1} - \mathbf{P}_1)\mathbf{a}_{nm} = (n - m)(\mathbf{a}_1 - \mathbf{a}_2). \quad [1]$$

It is clear that only pairs of vectors $(\mathbf{a}_{nm}, \mathbf{a}^*_{nm})$ related by the mirror operator P and hence different only in the sense of permutation of indices will satisfy this condition. They enclose an angle $\theta = 2\eta_1$ given by the formula

$$2\eta_1 = 2 \arctan\left[\frac{\sqrt{3}}{3}\left(1 - \frac{m}{n}\right)\Big/\left(1 + \frac{m}{n}\right)\right], \quad [2]$$

which is the twist angle of the boundary. Notice that in the case of small misorientation angles $\theta = 2\eta$, when the approach in terms of dislocations is still valid, the value of $\mathbf{r}$ in Eq. [1] for a real space lattice coincides with that of the Burgers vector $\mathbf{b}$ of screw dislocations separated by the distance D (i.e., equal to a_{nm}). Therefore the scalar form of [1], $\sin\theta/r = \sin(90^\circ - \delta)/a_{nm}$, transforms as $\delta \to 0$ into the

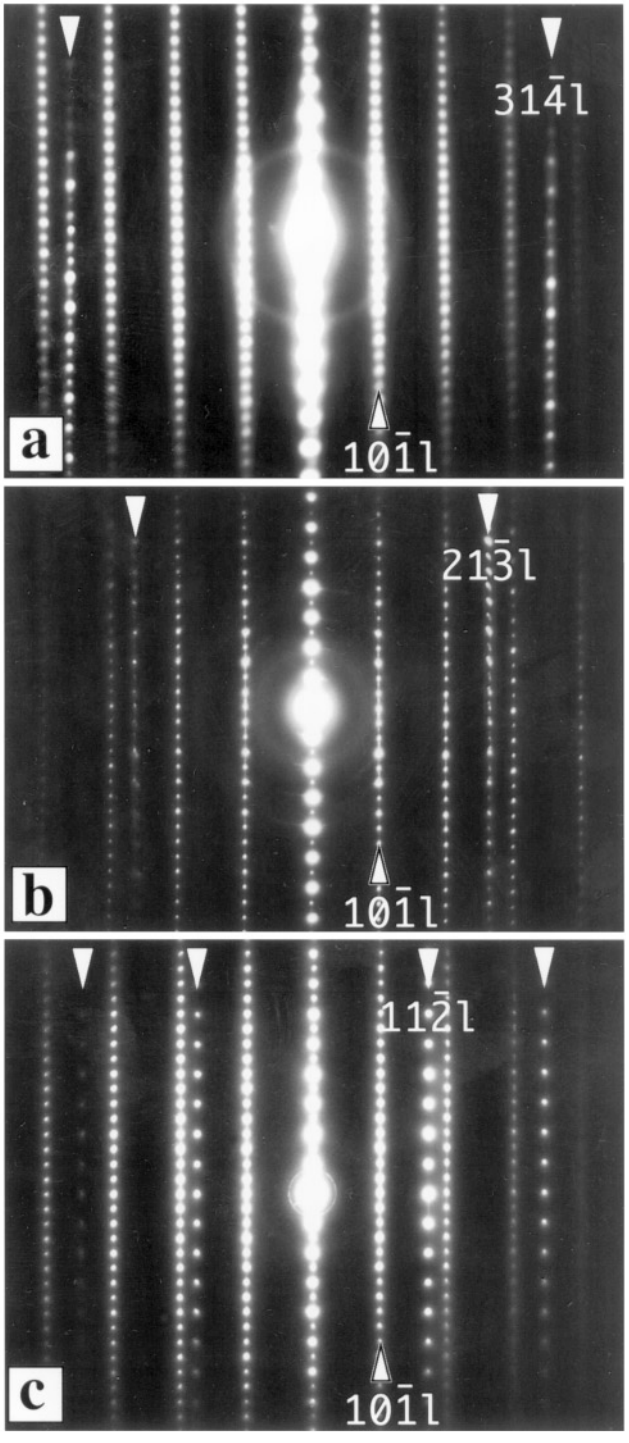

FIG. 8. Cross-section ED patterns of different rotation twins with common *c*-axis found in $TaReSe_4$: (a) 13–14° R-twins; (b) 17–18° R-twins; and (c) 25–27° R-twins. Notice that the rows of reflections (101$\bar{1}$) of the first crystal and those (h1h + $\bar{1}\bar{1}$) of the second one do not lie exactly in one projected plane. Therefore a relative intensity of the neighboring rows of spots in DP changes in opposite way for two crystals forming twist boundaries.

formula $\sin\theta/b = 1/D$, which leads to the well-known formula for screw dislocations $\sin\theta = \theta = b/D$.

When considering another set of vectors $\mathbf{a}_{nm}$ and $\mathbf{a}^*_{nm} = \mathbf{P}_2\mathbf{a}_{nm} = n\mathbf{a}_1 + m(\mathbf{a}_1 - \mathbf{a}_2)$ related by the mirror plane P_2 (parallel to $\mathbf{a}_1$ or equivalent-parallel to $\mathbf{a}_2$ in Fig. 11), a condition similar to [1],

$$\mathbf{r} = \mathbf{a}_{nm} - \mathbf{a}^*_{nm} = (\mathbf{1} - \mathbf{P}_2)\mathbf{a}_{nm} = m(2\mathbf{a}_2 - \mathbf{a}_1), \qquad [3]$$

leads to another enclosed angle $\theta = 2\eta_2$ given by

$$2\eta_2 = 2\arctan\left[\sqrt{3}\left(\frac{m}{n}\right)\Big/\left(2 + \frac{m}{n}\right)\right]. \qquad [4]$$

Notice that n and m in [1] and [3] should be integers, since $(\mathbf{a}_1 - \mathbf{a}_2)$, $(2\mathbf{a}_2 - \mathbf{a}_1)$ and $\mathbf{r}$ are the base vectors of the hexagonal lattice. The detailed derivation of the equations [2], [4] is given in the Appendix. It is clear that the angle $\theta = 2\eta$ in [2], [4] depends only on the ratio (m/n). The equations [2], [4] may lead to the same angles for different ratios $q_1 = m_1/n_1$ and $q_2 = m_2/n_2$ provided $q_1 + 2q_1q_2 + q_2 = 1$.

The last condition is obtained by putting $\eta_1 = \eta_2$. However, the same value of q_1 and q_2 cannot lead to the same η-angle in [2], [4], because $2q^2 + 2q - 1 = 0$ has no rational solution. On the other hand, the same value of the η-angle in [2], [4] is equivalent to the condition

$$\frac{m_2}{n_2} = \left(\frac{1 - m_1}{n_1}\right)\Big/\left(\frac{1 + 2m_1}{n_1}\right) \quad \text{or} \quad q_2 = \frac{1 - q_1}{1 + 2q_1}, \qquad [5]$$

which makes it possible to find the twin relations between the reflections in reciprocal space, generated by P_1 and P_2 mirror operators for the same θ angle. Assuming only positive rational values of q_1 and q_2, it is easy to find that they can change within the corresponding ranges $0 < q_1 < 1$ and $1 > q_2 > 0$. Some examples of the calculated twist boundaries with different rotation angles $\theta = 2\eta$ are shown in Figs. 7c and 7d and Fig. 12. Notice that these patterns can be used for both real and reciprocal space analysis. In the latter case, however, additional "superstructure" reflections, not shown in these patterns, will appear because of the commensurate character of the superlattices created. The density of coincidence points is obtained by determining the surface area of the unit mesh of the lattice formed by CSL. The base vectors of the CSL $\mathbf{a}_{nm}$ have a length given by $a^*(m^2 + n^2 + mn)^{1/2}$ and enclose an angle of 60°. The surface area is thus $a^{2*}(n^2 + m^2 + nm)\sqrt{3}/2$, whereas the surface area of a unit mesh of the lattice is $a^2\sqrt{3}/2$. The inverse of the CSL density is thus $N = (n^2 + m^2 + nm)$. Note that this expression depends on the absolute values of m and n and not only on the ratio m/n. This means that the same rotation angle can be realized for different pairs (m, n)

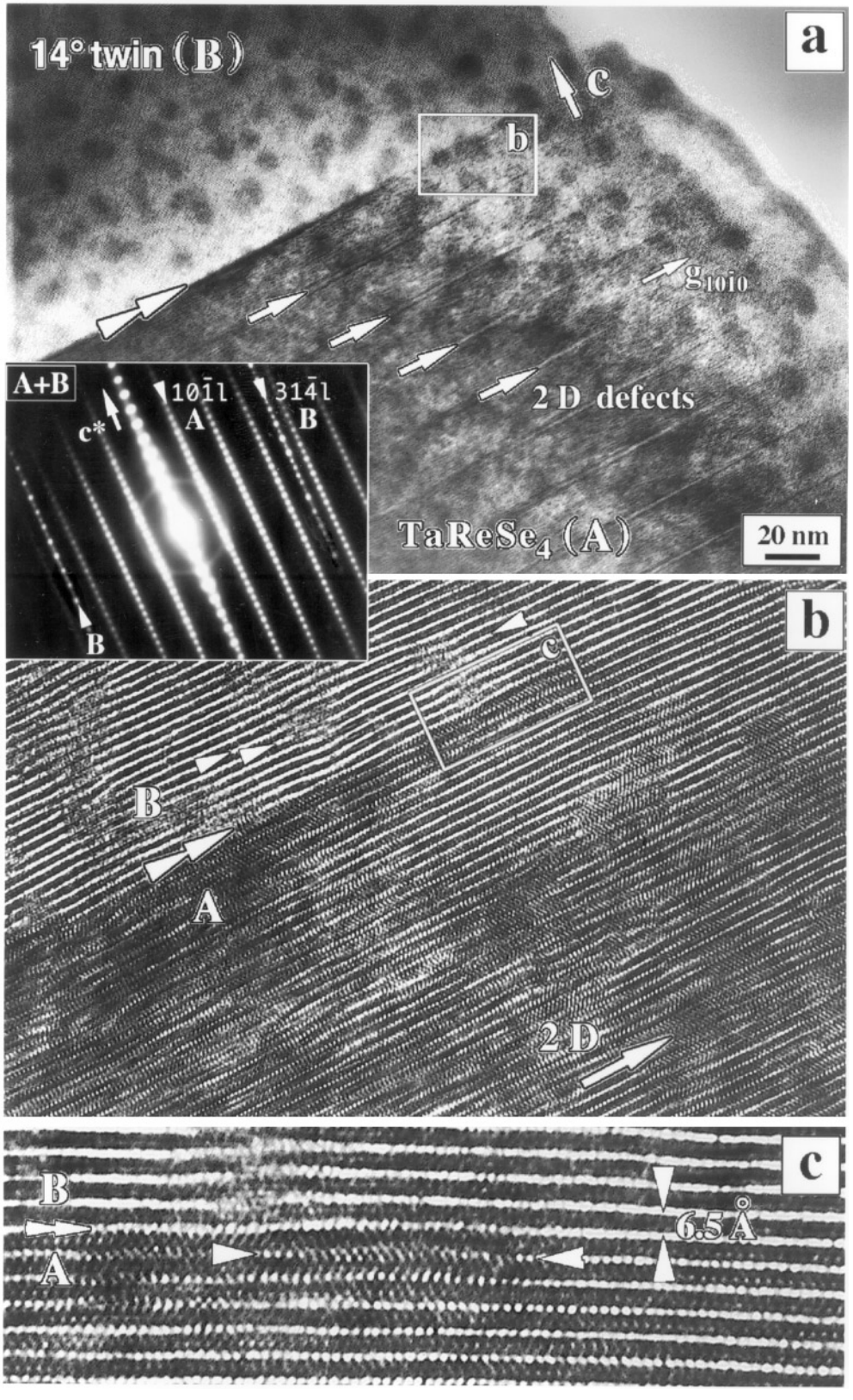
14° twin (B)
a
c
b
$g_{10\bar{1}0}$
2 D defects
TaReSe$_4$ (A)
20 nm
A+B
c*
$10\bar{1}1$
A
$31\bar{4}1$
B
B
b
c
B
A
2 D
c
B
A
6.5 Å

provided the ratio m/n remains the same. Let $n = kn'$ and $m = km'$, where k is an integer as well as n' and m'. Then for the twist angle, corresponding to $m/n = m'/n'$, the value N is then $k^2(n'^2 + m'^2 + n'm') = k^2N'$. The base vectors of CSL then become $\mathbf{a}_{n'm'} = n'\mathbf{a}_1 + m'\mathbf{a}_2 = (1/k)(n\mathbf{a}_1 + m\mathbf{a}_2)$. It means that the originally chosen CSL in fact has internal coincidence sites and therefore a smaller unit mesh can be chosen. The reduced value N' is the true value of the reciprocal CSL density. The boundary energy hence will increase with increasing value of N'.

The "magic" angles of R-twins calculated from formulae [2]–[4], the inverse CSL density N' of the twist boundaries corresponding to these angles, and the experimentally observed rotation angles in TRS are collected in Table 2. It is clear from this table that all magic angles correspond to the formation of CSL or, in other terms, to 2-D superstructures determined by $\mathbf{a}_{nm}$ vectors. The inverse CSL density N' is a strongly oscillating function of angle θ. Therefore the formation of the most stable superstructures is expected to occur only for certain angles with the deepest minima of this function $N'(\theta)$. As one can see from Table 2, the latter occur each time, a minimal $\mathbf{a}_{nm}$ is generated by the interchange of $P_1 \leftrightarrow P_2$ mirror operations. This conclusion is consistent with the experimentally found angles for TRS (Table 2). Notice that a perfect superstructure DP was experimentally found only for 21.8° R-twins. This exactly corresponds to the absolute minimum value of $N'(21.78^\circ) = 7$. The actually observed angles of other R-twins slightly differ from those given in Table 1, implying the formation of nearly commensurate DP and HREM images, as it is shown in Fig. 5. The largest angular mismatch from the predicted ones was found only for 25°–27° R-twins. We believe that even in this case (Fig. 7a), the definite angular orientation of the lamellae is governed by the weak VDW-bonds via the defect narrow interface (Fig. 10c) in the attempt to minimize value of N'. Coming back to the two mirrors model, it is clear that the patterns in Figs. 7c, 7d, 12 reflect the symmetry of the twist boundaries or, in other words, the symmetry of the associated reconstructed interfaces. For instance, the (7×7) or (5×5) reconstructed interfaces in terms of the "two mirrors model" correspond to the cases of 9.4° and 13.2° R-twins, respectively (Fig. 12). An example of a model interface in TRS corresponding to 13.2° R-twins, its diffraction pattern, and the calculated images are shown in Fig. 13. Notice that the approach used in the two-mirrors model, is very general. Therefore the mathematical formalism developed can be extended easily to all other types of interfaces based on 2-D lattices containing mirror planes.

3.4.3. 2-D defect planes. Another type of defects, so-called 2-D defect planes, was found to be the most frequent one. An example is shown in Fig. 9a. Notice that the linear density of these defect interfaces or stacking faults along the c-axis can be as high as $\sim 10^5$–10^6 cm^{-1} and cannot be explained by the simple presence of impurities. In many cases a nearly periodic sequence of defect planes was observed forming a quasi superstructure along the c-axis (Fig. 9a). Notice that such 2D-defects can be observed only under specific diffraction contrast conditions such as were used in Fig. 9a, and become invisible in the exact zone orientation used for HREM imaging. Analysis of diffraction contrast images in two beam conditions made it possible to conclude that such 2-D defects are characterized by a partial displacement vector of $R = (a/3)\langle 1\bar{1}00\rangle$ type. An example of an off-axis image of such planar defects is shown in Figs. 13a and 13b. Notice the increase of their density (Fig. 14a) approaching the $TaReSe_4/ReSe_2$ interface boundary. Attempts to image the 2-D defects on the atomic scale along $[01\bar{1}0]$ and $[11\bar{2}0]$ HREM directions within the instrumental resolution of the microscope were unsuccessful, because on the HREM-image plane the R vector has a projection of 0.95 Å only. On the other hand, such defects can still be revealed along with the one-dimensional lattice fringes displaying the thickness of MSe_2 sandwiches along the c-axis, 6.5 Å, when using a mixed, off-axis diffraction contrast and high-resolution imaging (Fig. 14b). In the latter case 2-D defects are always accompanied or associated with the loss of 2-lattice fringe periodicity, corresponding to the 13 Å thickness of the $2H_b$-polytype cell along the c-axis. This means that 2-D defects can be associated in general with stacking faults of lateral width 6.5 Å or 3×6.5 Å.

As mentioned above, a small admixture of $ReSe_2$ phase ($< 2\%$) in the material was found and successfully identified only by local chemical and SAED patterns analysis. In spite of the triclinic symmetry of $ReSe_2$ ($a' = 6.7272$, $b' = 6.6065$, $c' = 6.7196$ Å, $\alpha' = 118.94^\circ$, $\beta' = 91.83^\circ$, $\gamma' = 104.93^\circ$, Space group $P1$ (15)), its lattice parameters satisfy the necessary epitaxial relations well enough to form a natural $TaReSe_4/ReSe_2$ heterostructure. The orientation relations deduced from the ED analysis of bicrystals show, that the (b', c') plane of $ReSe_2$ is parallel to the (0001) $TaReSe_4$, the axes $b' \approx c' \approx 2a$ and coincide with those of the main phase,

FIG. 9. Cross-section images of the twist boundary formed by 14° R-twins: (a) Off-axis medium magnification bright-field image in reflection $\mathbf{g}_{10\bar{1}\bar{0}}$. The positions of the twist boundary and those of the 2-D defect planes are marked with arrows. (b) High resolution image of the selected b-area in (a) viewed along the $[0\bar{1}10]$ direction with respect to the A crystal. Notice the highly perturbed character of the local atomic structure. The expected position of the 2-D defect plane in the image of the A crystal is marked by an arrow, but its specific details in the HREM image are lost in the exact $[01\bar{1}0]$ orientation. (c) high magnification of the selected c-area in (b) HREM image of A/B twist boundary. The atomic matching at the A/B interface is evident (marked by double arrow). The fragment of a single VDW gap subjected to local self-intercalation by heavy cations is marked by joining arrows.

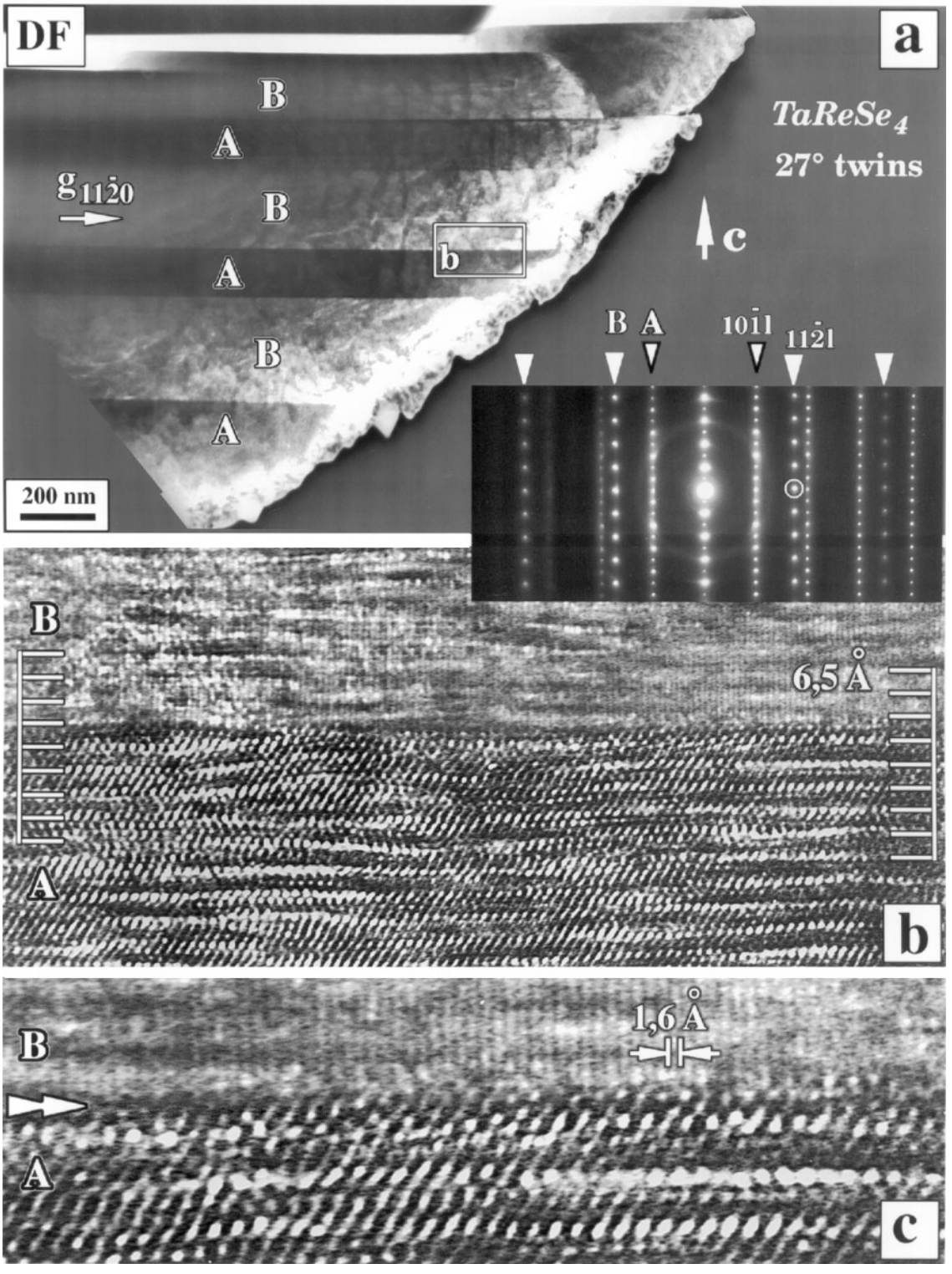

FIG. 10. Cross-section images of 27° R-twins: (a) Dark field image in $\mathbf{g}_{11\bar{2}0}$ reflection and (b) low magnification HREM image of A/B twist boundary; (c) high magnification HREM image of the same boundary. Inset is the ED pattern of the twist boundary.

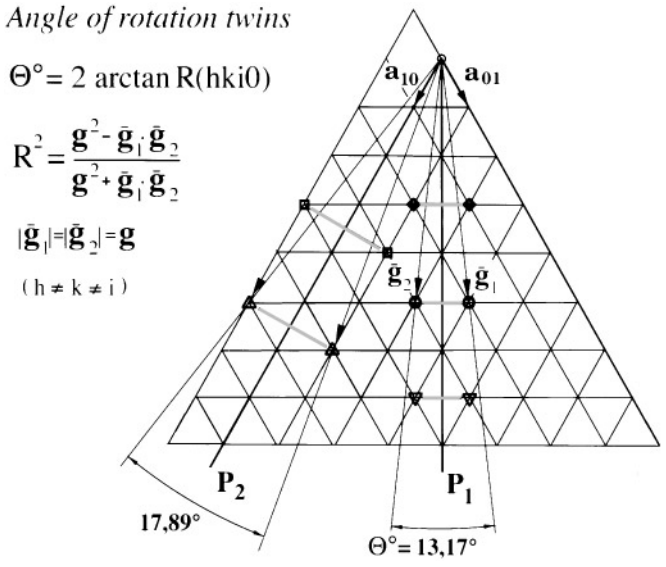

FIG. 11. Graphical illustration of the concept of the two mirrors model. Mirror planes of hexagonal lattice are marked by $\mathbf{P_1}$ and $\mathbf{P_2}$ lines. Two examples of superlattice vectors, generating 13.17° and 17.89° R-twins with respect to P_1 and P_2 mirrors, are highlighted.

the projection of the a'-axis onto [0001] $TaReSe_4$ is equal to $\approx c/2$, $\alpha' \approx \gamma = 120°$, where a, c and γ refer to the hexagonal structure of TRS. The presence of natural $TaReSe_4/ReSe_2$ interfaces was also revealed by direct HREM imaging. Indeed, the $ReSe_2$ phase can be considered as a superstructure with $Z = 4$ derived from the 1T-CdJ_2 structure ($Z = 1$) by doubling the a-lattice parameter, which in turn is related to the $2H_b$-MoS_2 structure type by the displacement $R = (a/3)\langle 1\bar{1}00\rangle$ applied to one of two Se layers forming MSe_2 sandwiches in the TRS structure. Notice that the driving force for the clustering of four Re atoms in the $ReSe_2$ structure is the antiferromagnetic coupling of initially uncoupled $3d$ electrons $(t_{2g})^3$ of each Re(4 +) resulting in the formation of direct Re–Re metal bonds in the $ReSe_2$ structure.

3.4.4. Other local and extended defects. The most characteristic types of local 0-D or 1-D defects are shown in Fig. 3 and Fig. 15a. Notice that they have a tendency to agglomerate in a cascade-like configuration (Fig. 3, Fig. 15a), since such defect regions decrease the overall strain energy of a highly defected layered crystal. We shall call them X- and Y-defects, since they are characterized by different Burgers vectors. The X-type defect has a glide component along the (0001) plane leading to the formation of a specific column-like defect configuration along the c-axis, as is shown in the HREM image of Fig. 3 (bottom inset). This illustrates the case of a VDW gap in which trigonal prismatic coordination by Se atoms (columns of white dots) is present. It is suggested that this specific configuration results from glide of one MSe_2 sandwich over another with a displacement vector of $R = (a/3)\langle 1\bar{1}00\rangle$ type (X-structure in Fig. 16). The formation energy of these defects may be relatively high because of the repulsion of Se atoms forming the VDW gap. However, it can be reduced when accompanied by metal intercalation in the VDW gap with a partial charge transfer, stabilizing the structure. For instance, a number of related intercalated A_xMX_2 compounds with $X = S$, Se ($x < 0.66$; A = Li, K, Na; M = Nb, Ta; or $x = 0.5$; A = Li, Na, K, Rb, Cs; M = Mo, W) was reported in (16), where the column-like structures formed by the columns of Se atoms (ζ- and η-structure models) have been suggested on the basis of experimental X-ray data. Notice that the X-type of defect configuration is particularly suited for trigonal prismatic coordination of the metal cations, Ta atoms, for instance, being intercalated into the gap.

Another most frequent type of local defects, i.e., Y-defects, is of the prismatic dislocation type with its main displacement vector having a component along the c-axis. It is presumably caused by the local self-intercalation of heavy cations, for instance Re atoms into the VDW gap; this does not change its octahedral coordination (Fig. 3). When the displacement vector $\mathbf{R}$ of the Y-defects exceeds the value of $(c/2)$[0001] another process of planar diffusion growth of extra lamellae (MSe_2 sandwich layers) can start to develop. For instance, one can compare the atomic core structure of the extended defect in Fig. 15c (inset) with that of the Y-defect in Fig. 15a. This process can have a different evolution from a simple planar prismatic defect (e) to a more complex step-like prismatic defects (c, d), where the extra lamella is always surrounded by an edge dislocation. The case shown in Fig. 15c can also be imagined as a collapse of two nearby prismatic defects in cascade-like configuration.

An interesting question arises when analyzing the stacking sequence of lamellae, forming the $2H_b$-structure polytype, outside of the defect cores shown in Figs. 15b–15d. Indeed, by assuming that the right hand side of these images corresponds to a perfect crystal, the tracing of lamellae fringes formally leads to a wrong stacking sequence of lamellae on the left side of the defects (highlighted by the left side and right side arrows). The assumption of intergrowth of $3R$ and $2H$ polytypes should be rejected, since computer simulations predict in this case the occurrence of streaks in the DP along $(10.l)$ and $(20.l)$ rows of spots with $l = 1, 2, 3, \ldots$, which are not experimentally observed. Hence, it is necessary to assume that either the structure of odd and even lamellae (or MX_2 layers) crossing the core of defects is interchanged, preserving the perfect structure outside of the defects, or it does not change at all. The former case means that (x, y) atomic coordinates of Me and Se atoms in each MX_2 layer crossing the core have to be replaced. However, it is not clear why the similar mirror-like lamellae just above and below the defect cores do not change their structure as

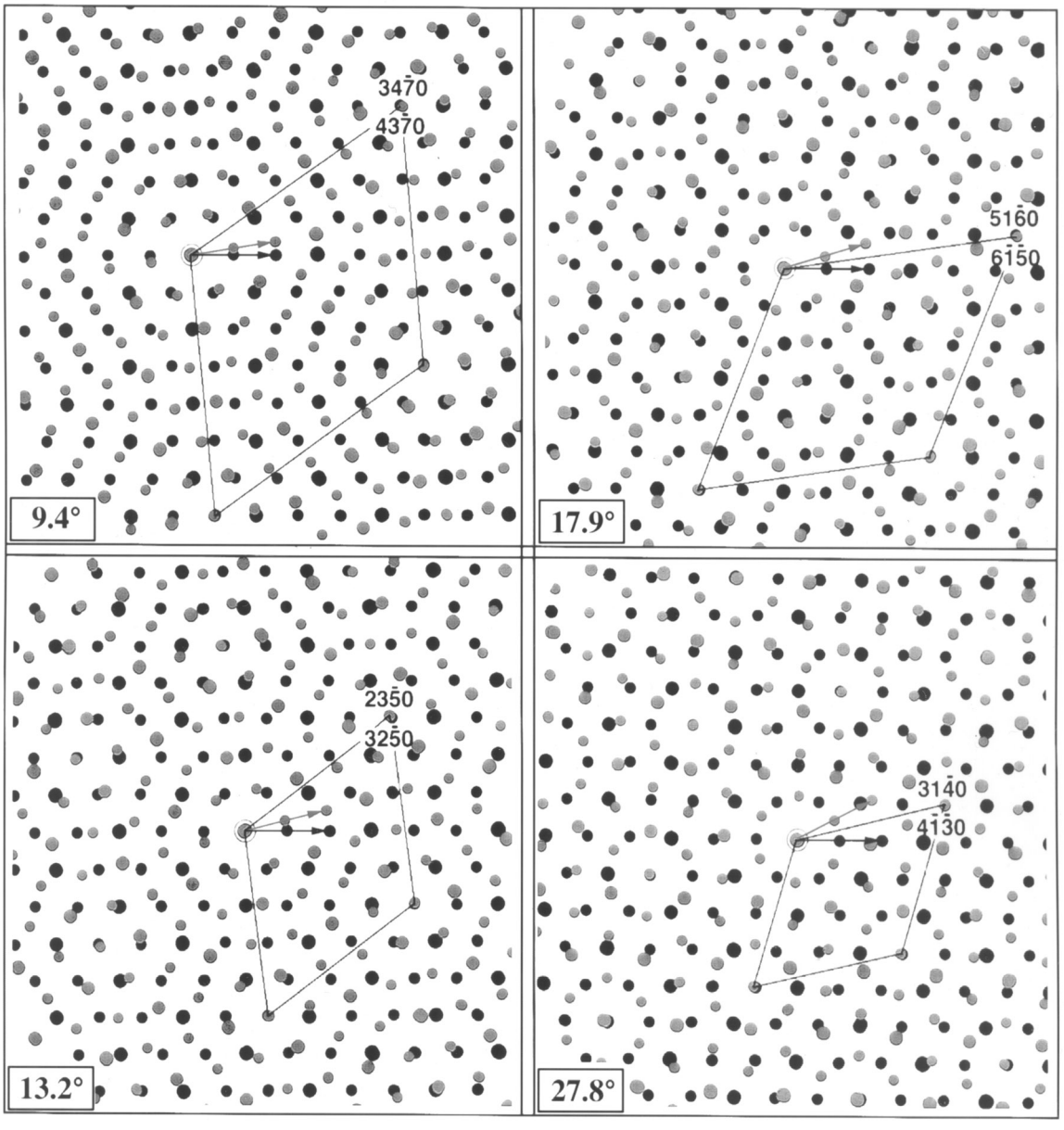

FIG. 12. Some examples of calculated twist boundaries forming commensurate 2-D superstructures (in real space). The parameters of generated R-twins are given in Table 2.

well. In the second case we formally arrive at an η-type of "column-like" structure ($a\ \gamma\ a$, $a\ \gamma\ a$) [16] similar to our X-defects observed above. However, the η-structure should lead to the formation of planar 2-D defects with the main component of the displacement vector of $\mathbf{R} = (\mathbf{a}/3)\langle 1\bar{1}00\rangle$ type. We will term this the paradox of odd and even planes. Notice that the η-type defect configuration is expected to be stabilized only by metal intercalation (for instance, of Ta atoms) into the trigonal prismatic VDW gap. Therefore it may form highly disturbed 2-D planes, acting as a getter or as an internal surface attracting interstitial (nonstoichiometric) metal atoms. Notice that the HREM images quite often show a highly disturbed character of (0001) planes in the areas where 2-D defects are expected to occur on the basis of the off-axis diffraction contrast image analysis. An example of such a HREM image with the expected 2-D defect position is shown in Fig. 9b (marked by arrow). To what extent the highly disturbed character of the 0001 lattice fringes must be attributed to the use of ion beam milling is unclear as yet.

TABLE 2
Experimental Angles of R-Twins in $TaReSe_4$ and Those Calculated from Two Mirrors Model

P_2 mirror:		P_1 mirror:					
R-twins	$q_2 = m_2/n_2$	R-twins	$q_1 = m_1/n_1$	$R = \tan(\theta^\circ/2)$	Inverse CSL density, N'	Rotation angle, θ°	Experimental angle, θ°
(3.1.0), (4. − 1.0)	1/3	(5.2.0), (2.5.0)	2/5	$\sqrt{3}/7$	**13**	27.79	25.5(3)
(4.1.0), (5. − 1.0)	1/4	**(2.1.0)**, (1.2.0)	1/2	$\sqrt{3}/9$	**7**	21.78	21.8
(5.1.0), (6. − 1.0)	1/5	(7.4.0), (4.7.0)	4/7	$\sqrt{3}/11$	**31**	17.89	17.5(2)
(6.1.0), (7. − 1.0)	1/6	(8.5.0), (5.8.0)	5/8	$\sqrt{3}/13$	43	15.18	
(7.1.0), (8. − 1.0)	1/7	**(3.2.0)**, (2.3.0)	2/3	$\sqrt{3}/15$	**19**	13.17	14.5(3)
(8.1.0), (9. − 1.0)	1/8	(10.7.0), (7.10.0)	7/10	$\sqrt{3}/17$	73	11.63	
(9.1.0), (10. − 1.0)	1/9	(11.8.0), (8.11.0)	8/11	$\sqrt{3}/19$	91	10.42	
(10.1.0), (11. − 1.0)	1/10	**(4.3.0)**, (3.4.0)	3/4	$\sqrt{3}/21$	**37**	9.43	9.1(2)
(11.1.0), (12. − 1.0)	1/11	(13.10.0), (10.13.0)	10/13	$\sqrt{3}/23$	133	8.61	
(12.1.0), (13. − 1.0)	1/12	(14.11.0), (11.14.0)	11/14	$\sqrt{3}/25$	157	7.93	

4. DISCUSSION

As mentioned above, the material is of practical interest because of its excellent lubricant properties. On the other hand, it is a degenerate semiconductor with a resistivity of 0.26 Ohm cm and effective carrier concentrations of (1–2) $\times 10^{18}\,cm^{-3}$ with mobility (10–30) $cm^2\,V^{-1}\,s^{-1}$ at room temperature [8]. As one can see from the analysis made above, the microstructure of TRS was of particular interest. The different types of defects were analyzed predominantly by electron microscopy methods, since X-ray data (Fig. 4) only provide information on the average structure of the material.

For unambiguous answers to some of the questions raised in this study, i.e. the formation mechanism of the unusual R-twins and 2-D defects, the paradox of odd and even planes, and some others, further analysis and additional experimental results will definitely be needed. However, at this moment we can already propose several reasonable assumptions. First, the presence of an admixture ($< 2\%$) of $ReSe_2$ suggests that the main phase should contain an excess of Ta with respect to Re at high temperatures, where the region of homogeneity of $TaReSe_4$ in the section $TaSe_2$–$ReSe_2$ of the phase diagram is expected to be asymmetrical and wider than at ambient conditions. Therefore an excess of Ta can result in the precipitation of $TaSe_2$ from the $TaReSe_4$ matrix on cooling because of narrowing of the homogeneity region as a function of temperature. Second, for $TaSe_2$ both of the $2H_a$ (17, 18) and 1T structure polytypes [19] have been reported. Both of them perfectly match epitaxially to the $TaReSe_4$ matrix. Apart from the version mentioned above, it can give an explanation for the formation of nondisturbed 2-D defect planes with displacement vector $\mathbf{R} = (\mathbf{a}/3)\langle -1100\rangle$ observed in this TEM-HREM study. Indeed, the displacement vector R applied to one of the Se-sublayers results in a 1T-structure configuration at the 2-D defect planes (Fig. 16). Notice that the expected density of such 2-D defects derived from the composition balance analysis ($\sim 2\%$) gives an estimate of 3×10^5 defects/cm along the c-axis, which agrees with the experimental data. Finally, we cannot exclude the possibility that 2-D defects may occur as single lamellae of $ReSe_2$ sandwiches as well, since their presence would cause the same displacement of one of the Se sublayers (Fig. 16). It is clear that all these features could result in the formation of 2-D precipitates similar to so-called Guinier–Preston zones first found in metal alloys. Glide by single partial dislocations in $TaReSe_4$, however, is less probable for several reasons. For a correct choice of the unique model of the 2-D defects a further local nanoscale chemical analysis of the 2-D defect composition would be required.

Notice that the presence of the 2-D defect planes leads to a spatial separation of the perfect glide dislocations into different slabs along the c-axis. They cannot intersect when moving in different glide planes along basal planes and therefore dislocation hardening of the material is unlikely to occur. The Peierls force of these dislocations must be very small, since their easy movement was observed *in situ* and already at room temperature by TEM experiments. In other words, this results in high plasticity and lubricity of this (TRS) material.

In spite of the high density of defects the experimental DP are nearly perfect and, in particular, do not contain streaks. For the explanation of this phenomenon we have to take into account that all the defects discussed above except the R-twins have displacement vectors, which just move the atoms both in the cation and in the anion sublattice of TRS from one Wyckoff position to another without changing the extinction conditions.

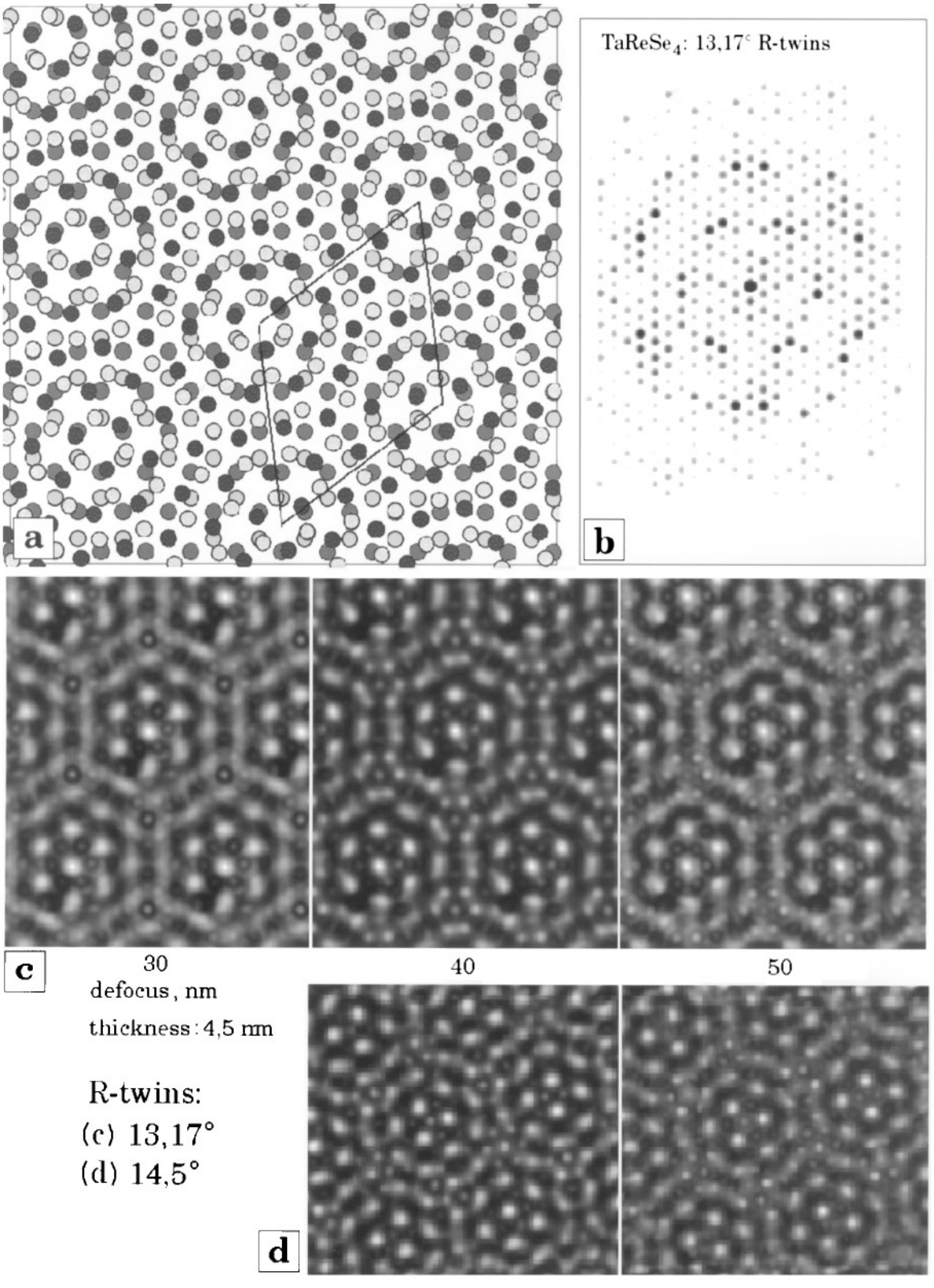

FIG. 13. An example of the results of theoretical calculations for 13.17° R-twins: (a) model of interface structure of TaReSe4 produced by rotation of the basic structure over a 13.17° angle, (b) calculated [0001] diffraction pattern, (c) and (d) examples of calculated HREM images for the twist boundaries forming the angles of 13.17° (predicted) and 14.5° (experimental one).

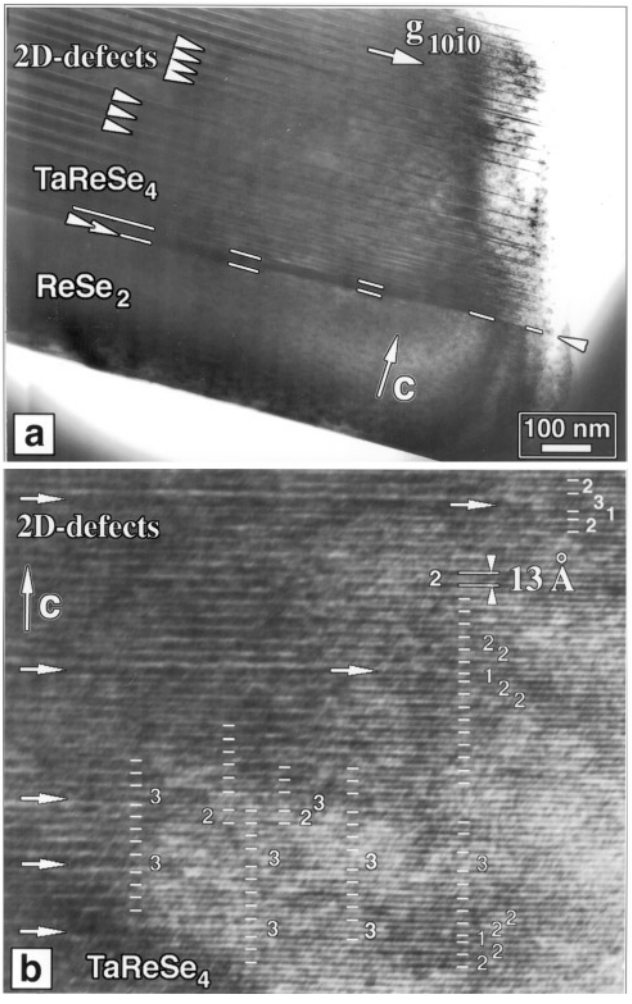

FIG. 14. Off-axis bright field image of $TaReSe_4$ in $\mathbf{g}_{10\bar{1}0}$ reflection: (a) natural bicrystal of $TaReSe_4/ReSe_2$ with positions of 2-D defect planes and bicrystal interface indicated with single and double arrows; (b) high magnification image of 2-D defects in mixed (diffraction and HREM) contrast. Notice that in such a crystal orientation the residual contrast image of 2-D defects is accompanied always by the breaking of the 2-fringes periodicity of a perfect crystal structure of the $2H_b$–$TaReSe_4$ polytype, implying that the thickness of 2-D defects may be either $6.5\,\text{Å} \times 1$ or $6.5\,\text{Å} \times 3$ along the c-axis.

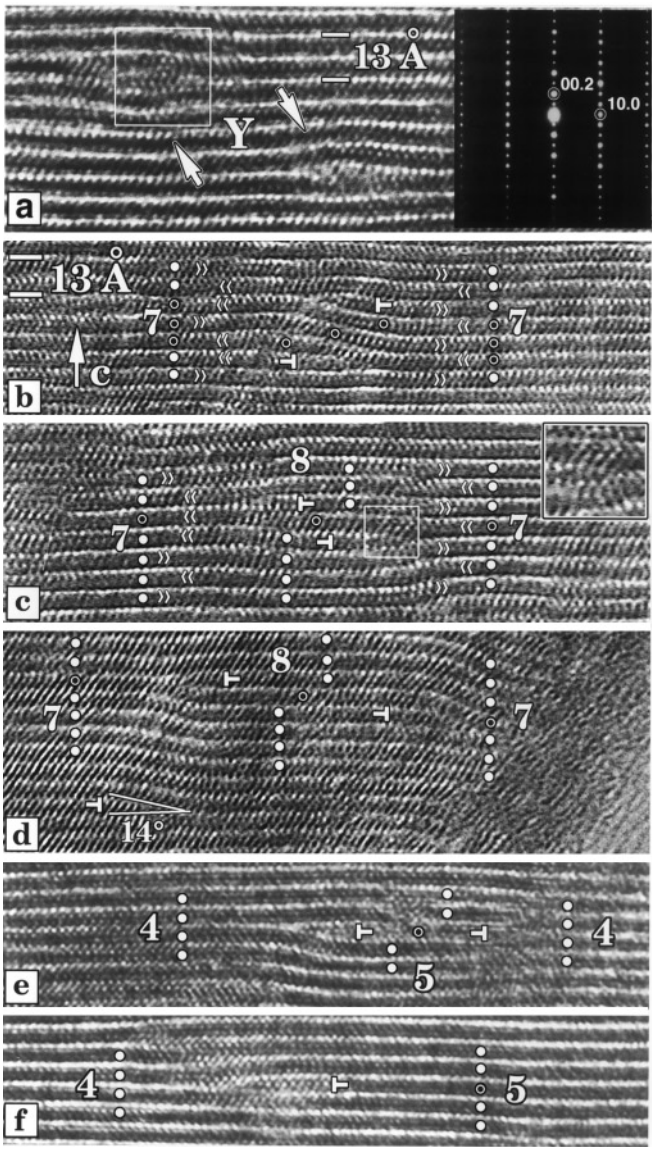

FIG. 15. Cross-section HREM images of a number of local and extended defects found in $TaReSe_4$: (a) Y-defects of a prismatic type caused by local self-intercalation of heavy metal atoms into the VDW gap; (b) core of a split dislocation; (c–e) nonplanar and planar Frank dislocation loop of prismatic type with Burgers vector equal approximately to $c/2[0001]$; (f) edge dislocation with the same Burgers vector.

According to our observations the main point of the rotation R-twins formation mechanism should take into account a reconstruction of the VDW gap governed by self-intercalation (or by intercalation) of heavy cations. If the intercalated atoms form an ordered superstructure already at high temperatures during crystal growth or phase transformation, the formation of R-twins will be very much simplified. In this case the ordered structure of intercalated atoms (or adatoms on the surface during crystal growth) might be determined by the formation of corresponding R-twins minimizing the twist boundary energy in a sense of CSL-density oscillations. The most suitable and therefore stable positions of intercalated atoms in the VDW gap are the trigonal prismatic ones, as was observed for a number of related intercalated A_xMX_2 compounds [16] forming the "column-like" η-structures discussed above. As one can see, the model structure of a twist boundary has indeed such positions at the vertices of the supercell shown in a plan-view in Fig. 13a, which reflect in the general case of R-twins the intermediate coordination polyhedra between the trigonal prismatic (stable in the 2H polytype) and the octahedral ones (stable

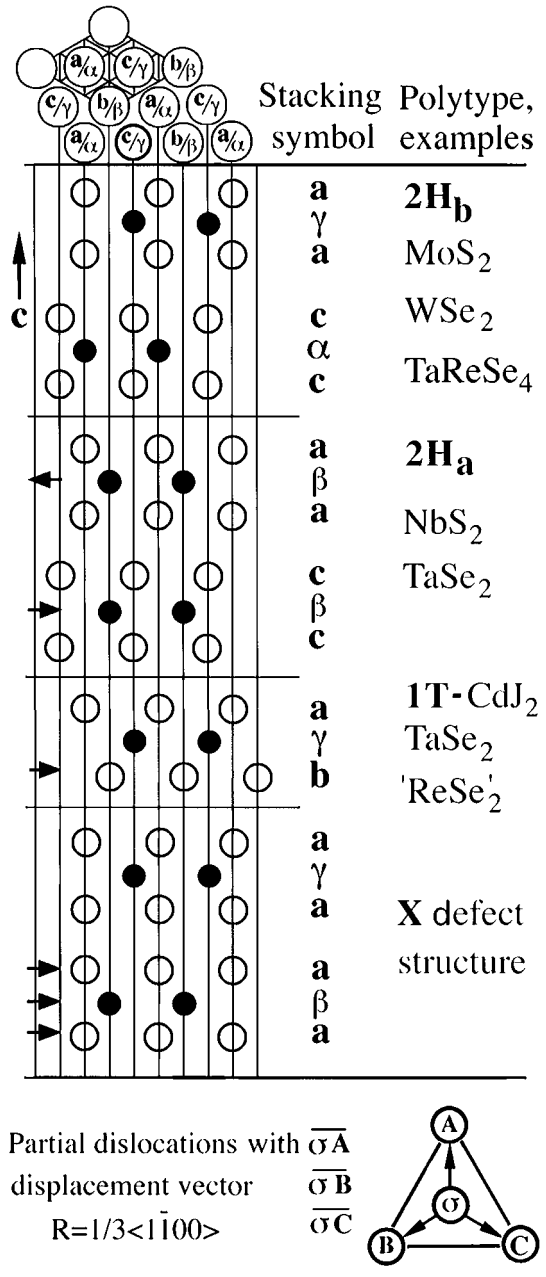

FIG. 16. Stacking modes of the different layered structures relevant to defect structures found in $TaReSe_4$.

in the 1T polytype). The local oversaturated concentration of metal atoms in each crystallite of $TaReSe_4$ would determine in this case a size and density of the most preferable reconstructed interfaces or 2-D superstructures formed by R-twins.

The driving force of twist boundaries formation may be related to the fact that Ta cations tend to be surrounded by trigonal prismatic coordination polyhedra of Se anions, whereas Re cations tend to occupy the centres of Se octahedra. If the distribution of Re and Ta is not random but rather nonuniform, Ta-rich layers may tend to form trigonal prismatic regions, whereas Re-rich layers would prefer to form octahedral configurations within MSe_2 lamellae. This may create torsion forces responsible for the disturbed character of TRS microstructure, as revealed with high sensitivity in HREM images.

5. CONCLUSION

The combined analysis of $TaReSe_4$ microstructure by several electron microscopy methods leads to an explanation of the excellent lubricant properties of $TaReSe_4$ and illuminates the role of the defect interfaces as microstructure in this process. The experimental and theoretical results on R-twins may give new insight into the nature of different intermediate superstructures and a key to the interpretation of the complex diffraction patterns found in layered dichalcogenides of transition metals by various authors.

APPENDIX

The close-packed directions OP and PQ (Fig. 17) of a close-packed arrangement of atom positions with lattice parameter **a** enclose an angle of 120° and form the vector OQ = OP + PQ. The lengths of its two components are taken as OP = ma and PQ = na. The mirror image of OQ with respect to the first family of mirror planes P_1 (Fig. 17b) is then OQ′ = OP′ + P′Q′, where P′ and Q′ again occupy lattice positions; as a result QQ′ is also a lattice vector.

The angle 2η (Fig. 17b) is the twist angle of the coincidence site lattice, generated by the rotation and superposition of two hexagonal lattices to make OQ and OQ′ coincide. The lattice parameter of the coincidence site lattice is then $\mathbf{a}(n^2 + m^2 + nm)^{1/2}$. The angle η can be calculated as follows. In the triangle OPQ one has

$$\sin\varphi/na = \sin(60^\circ - \varphi)/ma \qquad [A1]$$

This equation can be solved for φ as

$$\tan\varphi = \frac{\sqrt{3}}{2}\left(\frac{m}{n} + \frac{1}{2}\right). \qquad [A2]$$

From Fig. 17b it is clear that $\eta = (\varphi - 30^\circ)$ and hence

$$\tan\eta = (\tan\varphi - \tan 30^\circ)/(1 + \tan\varphi \tan 30^\circ). \qquad [A3]$$

With $\tan 30^\circ = \sqrt{3}/2$ this results

$$\tan\eta = \frac{\sqrt{3}}{3}\frac{n-m}{n+m}. \qquad [A4]$$

This is the formula (2) of Section 3.4.2.

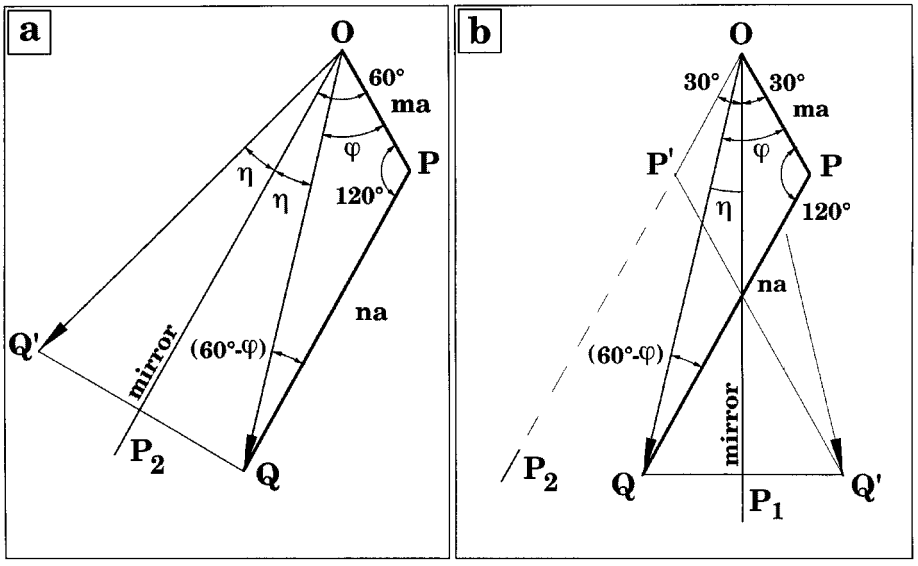

FIG. 17.

When the mirror image of the same line segments OP + PQ = OQ with respect to the second family of mirrors P_2 is considered (Fig. 17a), a similar reasoning can be followed; however, now $\eta = (60^\circ - \varphi)$. One now finds

$$\tan \eta = \sqrt{3}m/(m + 2n). \qquad [A5]$$

This is the formula [4] of Section 3.4.2. The two expressions [A4] and [A5] may lead to the same η for different ratios $r_1 = m_1/n_1$ and $r_2 = m_2/n_2$ provided $r_2 + 2r_1r_2 + r_2 = 1$. The last condition is obtained by putting $\eta_1 = \eta_2$.

ACKNOWLEDGMENTS

This research work was carried out in the framework of a Co-operation Agreement between the University of Antwerp, EMAT-RUCA, Belgium, and the N. S. Kurnakov Institute of General and Inorganic Chemistry, Russian Academy of Sciences, Moscow, Russia, and was partially supported by the Russian Foundation for Basic Research, Grant 96-03-33170. V. Volkov is grateful to the Belgian Science Policy Office for his DWTC fellowship in 1996.

REFERENCES

1. J. A. Wilson and A. D. Yoffe, *Adv. Phys.* **18,** 193 (1969).
2. A. H. Tompson and K. P. Pisharodi, *Phys. Rev. Lett.* **129,** 163 (1972).
3. V. L. Ginzburg, *Successes Phys. Sci.* **95,** 91 (1968). [In Russian]
4. R. Friend and A. D. Yoffe, *Adv. Phys.* **36,** 1 (1987).
5. G. V. Subba Rao, *in* "Intercalated Layered Materials," p. 99. Reidel, Dordrect, 1979.
6. S. Kuypers and J. Van Landuyt, *Mater. Sci. Forum* **100–101,** 223 (1992).
7. G. A. Wiegers and A. Meerschaut, *Mater. Sci. Forum* **100–101,** 101 (1992).
8. N. V. Elizarova, A. T. Falkengoff, V. V. Volkov, V. S. Pervov, B. M. Zhigarnovsky, E. V. Makhonina, and V. Yu. Kozhenkov, *Russ. J. Inorg. Mater.* **29,** 1069 (1993).
9. N. V. Elizarova, V. S. Pervov, A. T. Falkengoff, E. V. Makhonina, and B. M. Zhigarnovsky, *Russ. J. Inorg. Chem.* **39,** 1061 (1994).
10. K. Hayahi, M. Hyoma, H. Yamanaka, and H. Nishihara, *J. Less-Common Met.* **147,** 19 (1989).
11. W. Bollmann, *in* "Crystal Defects and Crystalline Interfaces," Ch. 13, p. 187. Springer-Verlag, Berlin/Heidelberg/New York, 1970.
12. F. M. Henry and K. Lonsdole, Eds., "International Tables for X-ray Crystallography," Vol. 1–3, p. 558. Kynoch, Birmingam, 1969.
13. F. Izumi, *in* "The Rietveld Method" (R. A. Young, Ed.), Ch. 13. Oxford Univ. Press, Oxford, 1993.
14. S. Amelinckx and P. Delavignette, "Electron Microscopy and Strength of Crystals" (J. Thomas and J. Washburn, Eds.), p. 441. Interscience, New York, 1962.
15. N. W. Alcock and A. Kjekshus, *Acta Chem. Scand.* **19,** 79 (1965).
16. W. Bronger, *in* "Crystallography and Crystal Chemistry of Materials with Layered Structures" (F. Lévy, Ed.), Vol. II, p. 93. Reidel, Dordrecht, 1976.
17. F. Jellinek, *J. Less-Comm. Met.* **4,** 9 (1962).
18. L. E. Conroy and K. P. Pisharody, *J. Solid State Chem.* **4,** 345 (1972).
19. E. Bjerkelund and A. Kjekshus, *Acta Chem. Scand.* **21,** 513 (1967).